J. Fluid Mech. (2011), *vol.* 673, *pp.* 513–547. © Cambridge University Press 2011. The online version of this article is published within an Open Access environment subject to the conditions of the Creative Commons Attribution-NonCommercial-ShareAlike licence <http://creativecommons.org/licenses/by-nc-sa/2.5/>. The written permission of Cambridge University Press must be obtained for commercial re-use.

doi:10.1017/S0022112010006361

Viscous effects on the oscillations of two equal and deformable bubbles under a step change in pressure

N. CHATZIDAI, Y. DIMAKOPOULOS AND J. TSAMOPOULOS†

Laboratory of Computational Fluid Dynamics, Department of Chemical Engineering, University of Patras, Patras 26500, Greece

(Received 28 May 2009; revised 14 October 2010; accepted 13 December 2010; first published online 1 March 2011)

According to linear theory and assuming the liquids to be inviscid and the bubbles to remain spherical, bubbles set in oscillation attract or repel each other with a force that is proportional to the product of their amplitude of volume pulsations and inversely proportional to the square of their distance apart. This force is attractive, if the forcing frequency lies outside the range of eigenfrequencies for volume oscillation of the two bubbles. Here we study the nonlinear interaction of two deformable bubbles set in oscillation in water by a step change in the ambient pressure, by solving the Navier–Stokes equations numerically. As in typical experiments, the bubble radii are in the range 1–1000 μm. We find that the smaller bubbles (∼5 μm) deform only slightly, especially when they are close to each other initially. Increasing the bubble size decreases the capillary force and increases bubble acceleration towards each other, leading to oblate or spherical cap or even globally deformed shapes. These deformations may develop primarily in the rear side of the bubbles because of a combination of their translation and harmonic or subharmonic resonance between the breathing mode and the surface harmonics. Bubble deformation is also promoted when they are further apart or when the disturbance amplitude decreases. The attractive force depends on the Ohnesorge number and the ambient pressure to capillary forces ratio, linearly on the radius of each bubble and inversely on the square of their separation. Additional damping either because of liquid compressibility or heat transfer in the bubble is also examined.

Key words: bubble dynamics, interfacial flows (free surface)

1. Introduction

Bubble dynamics plays a central role in several practical applications and physical phenomena and, hence, it has challenged researchers for many decades. Early on, Rayleigh (1917) described the collapse of a single bubble as a result of changes in the local pressure field, but in the absence of other surfaces in their vicinity. The violent collapse of cavities can cause high pressure, resulting in serious damage of nearby solid

† Email address for correspondence: tsamo@chemeng.upatras.gr

https://doi.org/10.1017/S0022112010006361 Published online by Cambridge University Press

surfaces. Often, the generation, stabilization or interaction of bubbles is enhanced by introducing a pressure wave or other disturbance in the host liquid. Bubbles, depending on their size, are trapped in pressure nodes (larger bubbles) or antinodes (smaller bubbles) of a standing pressure wave, feeling an effective force known as the primary Bjerknes force (Bjerknes 1906). There, owing to rectified diffusion of dissolved gases and volume pulsations, bubbles may grow until they eventually reach a state of dynamic equilibrium that is characterized by stable radial oscillations (Leighton 1994). These processes are part of what is called acoustic cavitation. Besides their interaction with nearby solid surfaces, bubbles also interact with each other as each bubble moves due to fluid acceleration caused by the volume oscillations of another bubble. This is the so-called secondary Bjerknes force, since it was first investigated by V. F. K. Bjerknes (1906, 1909). The primary and secondary Bjerknes forces were explained by postulating that every body that is moving in an accelerating fluid is subjected to a 'kinetic buoyancy', which is proportional to the product of the acceleration of the fluid, g, multiplied by the mass, ρV, of the fluid displaced by the body: $F \sim g\rho V$. Bjerknes (1906) hoped to use this phenomenon to explain the effects of electromagnetism and gravitation. The analogy with these forces was supported by the fact that, according to linear theory and assuming inviscid and incompressible fluids and bubbles that remain spherical, the secondary Bjerknes force is proportional to the product of the amplitude of volume pulsations of the two bubbles and inversely proportional to the square of the distance between their centres of volume. This force can be attractive or repulsive depending on whether the bubbles oscillate in-phase or out-of-phase, respectively.

On the basis of the reasoning that the primary Bjerknes force drives the bubbles to pressure nodes or antinodes, Crum (1975) used a stationary pressure wave in the vertical direction to counterbalance gravity. The induced volume oscillations generated bubble translation as well. He measured their relative velocity of approach in the horizontal direction and found that the secondary Bjerknes force is much smaller than the primary one. However, it can increase by increasing the frequency of the pulsations and consequently ultrasonic pressure variations can be used in separation processes in order to remove gases from gas/liquid dispersions (Batchelor 1967). Moreover, the secondary Bjerknes force is responsible for several interesting dynamic phenomena which, among others, include bubble coalescence, formation of stable bubble pairs that move together in the host liquid and the formation of satellite bubbles (Kornfeld & Suvorov 1944). More recently, the field of cavitation gained significant momentum, due to the remarkable phenomenon of single bubble sonoluminescence (Brenner, Hilgenfeldt & Lohse 2002; Lauterborn *et al.* 2007), which is associated with light emission during collapse of either a cavitating or a laser-induced bubble. During the last decade, there has been an emerging biomedical application of bubbles in the form of contrast agents, which are micron-sized bubbles that are encapsulated in a lipid polymer or albumin shell (Goldberg, Raichlen & Forsberg 2001; Tsiglifis & Pelekasis 2008). Controlled oscillations and collapse of such bubbles have also been used recently for enhanced drug and gene delivery (Li *et al.* 2003).

Over the past several decades, a significant amount of research has been devoted to the study of single bubble dynamics (see Plesset & Prosperetti 1977 and Feng & Leal 1997 for reviews on earlier and more recent work on the subject). For the problem of bubble–bubble interaction, efforts to evaluate the secondary Bjerknes force in the context of linear oscillations were reported by Zabolotskaya (1984) and later on by Doinikov & Zavtrak (1995) and Doinikov (1999), who included viscous

https://doi.org/10.1017/S0022112010006361 Published online by Cambridge University Press

effects on interacting spherical bubbles. More recently, Pelekasis *et al.* (2004) have made a systematic effort to evaluate the two available mechanisms that explain the formation of stable bubble clusters, when bubbles oscillate below resonance under an intense acoustic disturbance, extending the earlier work of Oguz & Prosperetti (1990) and Mettin *et al.* (1997). In this effort, the viscous boundary layers around each bubble were systematically accounted for, but the bubbles were still assumed to remain spherical because of the large interbubble distance compared to their radii. Earlier, Pelekasis & Tsamopoulos (1993*a*, *b*) reported a detailed study of the volume and shape oscillations of two bubbles assuming that the surrounding liquid is inviscid. This assumption is acceptable for a bubble radius larger than $\sim$1 mm. They examined a certain range of frequencies, pressures and pressure amplitudes, bubble sizes and distances. This is the only study to date in which the surface of each bubble was allowed to deform in response to capillary, pressure and inertia forces, while retaining their axial symmetry. The results of these simulations show agreement with linear theory with respect to the influence of the separation distance, volumes of the bubbles, forcing amplitude and frequency upon the average acceleration acquired by the bubbles in relative motion. An important nonlinear result is the fact that when the Bond number, $Bo=(\rho^*\langle g^*\rangle R^{*2})/\sigma^*$, based on the time-averaged bubble acceleration, $\langle g^*\rangle$, the bubble radius, R^*, and the properties of the liquid (density, ρ^*, and surface tension, σ^*), lies above a critical value, the bubble shapes resemble the spherical-cap shapes first reported by Davies & Taylor (1950) for steadily rising bubbles. On the contrary, when Bo lies below a critical value, globally deformed shapes appear, which have been reported by Kornfeld & Suvorov (1944). These shape instabilities arise because of harmonic or subharmonic resonance of the surface modes with the volume oscillations of the bubble, the so-called parametric instability. These instabilities more often arise on the back side of the bubbles, because of the stabilizing effect of the straining motion of the liquid adjoining the front bubble interface (Batchelor 1987). However, in Pelekasis & Tsamopoulos (1993*a*, *b*), due to the assumption of negligible viscous effects, the bubble motion and deformation could not be followed for very long as they approached each other due to very sharp shape distortions, possibly leading to premature bubble breakup. Another aspect that was not included was bubble coalescence, which is known to occur under cavitation conditions. The process of bubble coalescence was studied numerically, for example by Chen, Li & Manasseh (1998), in the context of rising bubbles using a control volume technique for the discretization of the surrounding fluid. The dynamic phenomena involved, however, in the interaction of cavitating or laser-induced bubbles are more severe and of different nature, in view of the large disturbances that are applied, thus requiring the more sophisticated numerical approach presented herein.

In the present work, the nonlinear interactions of two deforming bubbles of radius ranging between 1 μm and 1 mm will be examined. In contrast to the work of Pelekasis & Tsamopoulos (1993*a*, *b*), viscous effects will be accounted in full and the effect of liquid compressibility and heat transfer in the bubble will be examined as additional damping mechanisms. The two bubbles will be subjected to a step change in pressure at infinity, not an oscillatory one in order to avoid introducing another parameter in the present study. In § 2, we present the governing equations and boundary conditions of the problem. In § 3, we very briefly mention the numerical method of solution. The results in terms of the relevant eigenmodes and nonlinear bubble interactions for equal bubbles under a step change in the far-field pressure are presented in § 4. Finally, conclusions are drawn in § 5.

https://doi.org/10.1017/S0022112010006361 Published online by Cambridge University Press

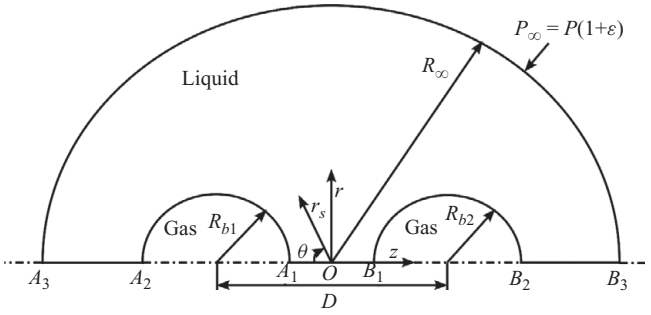

FIGURE 1. Schematic diagram of the flow geometry and the coordinate system of the problem.

2. Problem formulation

The motion and the nonlinear interactions of two equal gas bubbles surrounded by a viscous liquid are considered. Axial symmetry around the axis connecting the two bubble centres is assumed. The density and viscosity of the gas inside the bubbles is assumed to be much smaller than that of the liquid, which are ρ^* and μ^*, respectively, so that the gas is considered to be inertialess and inviscid. Therefore, its pressure varies only with time according to a polytropic law. Figure 1 illustrates a schematic of the flow geometry examined herein. The two bubbles are initially spherical with radius $R_{b1}^* = R_{b2}^* = R_b^*$, which is used as the length scale and distance D^* between their two centres of volume. Because of the absence of an explicit velocity, surface tension σ^* is used for making velocity, time and pressure dimensionless. Therefore, velocity is scaled with $(\sigma^*/R_b^*\rho^*)^{1/2}$, time with $(R_b^{*3}\rho^*/\sigma^*)^{1/2}$ and pressure with σ^*/R_b^*. The dimensionless number that arises is the Ohnesorge number, $Oh = (\mu^{*2}/\rho^* R_b^* \sigma^*)^{1/2}$. The importance of surface tension can be deduced directly because it is used to scale the initial hydrostatic pressure in the liquid, P^*.

Motion is induced by a step change in pressure far away from the bubbles, which means that for time greater than zero, the pressure at infinity is given by

$$P_\infty = P(1+\varepsilon), \tag{2.1}$$

where ε is the amplitude of the disturbance. The flow is governed by the momentum and mass conservation equations, which in their dimensionless form are

$$\frac{\mathrm{D}\boldsymbol{u}}{\mathrm{D}t} - \nabla\cdot\boldsymbol{\sigma} = 0, \tag{2.2}$$

$$\nabla\cdot\boldsymbol{u} = 0, \tag{2.3}$$

where $\boldsymbol{\sigma}$ is the total stress tensor,

$$\boldsymbol{\sigma} \equiv -P\boldsymbol{I} + \boldsymbol{\tau} = -P\boldsymbol{I} + Oh[\nabla\boldsymbol{u} + (\nabla\boldsymbol{u})^{\mathrm{T}}], \tag{2.4}$$

where $\boldsymbol{u}$ is the velocity vector, $\boldsymbol{\sigma}$ is the total stress tensor, P is the pressure in the liquid, ∇ is the gradient operator and $\boldsymbol{I}$ is the identity matrix. Along the free surface of the bubbles, the velocity field should satisfy a local force balance between the capillary forces, viscous stresses in the liquid and pressure inside the bubble:

$$\boldsymbol{n}\cdot\boldsymbol{\sigma} = -\boldsymbol{n}P_g + 2H\boldsymbol{n}, \tag{2.5}$$

where P_g is the pressure inside each bubble, $\boldsymbol{n}$ is the outward unit normal to its surface and $2H$ is its mean curvature which is defined as

$$2H = -\nabla_s\cdot\boldsymbol{n}, \quad \nabla_s = (\boldsymbol{I} - \boldsymbol{nn})\cdot\nabla. \tag{2.6}$$

https://doi.org/10.1017/S0022112010006361 Published online by Cambridge University Press

Moreover, along each bubble interface, the kinematic condition must be imposed:

$$\frac{\mathrm{D}\boldsymbol{F}}{\mathrm{D}t} = \boldsymbol{u}, \tag{2.7}$$

where $\boldsymbol{F}$ is the position vector of the interface, given by

$$\boldsymbol{F} = f_s \boldsymbol{e}_r, \tag{2.8}$$

where f_s is the radial distance to the bubble surface from the centre of the respective local spherical coordinate system and $\boldsymbol{e}_r$ the respective unit vector.

The gas inside each bubble is considered ideal and its pressure varies adiabatically with the instantaneous volume:

$$P_g = P_{go}\left(\frac{V_o}{V}\right)^{\gamma}, \tag{2.9}$$

where P_{go} and V_o are the initial pressure and the volume, V is the instantaneous volume of each bubble and γ is the polytropic constant that is assumed here equal to 1.4. The volume of each bubble is calculated in local spherical coordinates after each time step through

$$V = \frac{2\pi}{3}\int_0^{\pi} f_s^3 \sin\theta \mathrm{d}\theta. \tag{2.10}$$

Along the axis of symmetry, the usual symmetry conditions are applied. The infinite domain of the fluid around the two bubbles is truncated to a finite spherical domain with a radius R_∞, which is much larger than the bubble radii, so that this boundary does not affect the flow around the two bubbles. This is further facilitated by using the open boundary condition suggested by Papanastasiou, Malamataris & Elwood (1992). This condition is equivalent to extending the validity of the weak form of the governing equations to the outflow boundary, instead of replacing them with arbitrary boundary conditions there.

3. Numerical solution

These equations are solved numerically using the mixed finite element method to discretize the velocity and pressure fields, combined with an advanced elliptic grid generator for the initial construction and subsequent motion of the mesh points in the liquid domain. Details of this method applied in the present problem are given in Chatzidai *et al.* (2009), where a number of convergence tests have also been reported to determine (i) the number of elements required on the bubble surfaces in particular, to resolve the boundary layers that may arise in this problem and (ii) the radial distance, R_∞, of the far-field boundary condition. Through numerous tests, it was determined that setting $R_\infty = 30$ was more than sufficient to guarantee that the outflow boundary did not affect our results in any measurable way. This method has been applied successfully to a number of free- or moving-boundary problems (Dimakopoulos & Tsamopoulos 2003; Karapetsas & Tsamopoulos 2006; Foteinopoulou *et al.* 2006; Tsamopoulos *et al.* 2008). In Tsamopoulos *et al.* (2008), the steady rise and deformation of a bubble in a Newtonian or a viscoplastic material was studied and the accuracy of the present code was demonstrated, because its predictions for the bubble shape and rise velocity and the various geometric characteristics of the vortex behind it were found to be in excellent agreement with results of numerous earlier experimental and theoretical studies.

https://doi.org/10.1017/S0022112010006361 Published online by Cambridge University Press

Here particular problems that arise when simulations are carried out to long times are the corrugated bubble surfaces and the translation of the bubbles very close to each other. The first problem makes the discretization of the mesh coarser and coarser within the bubble troughs, while the second problem makes it unnecessarily fine in the area between the two bubbles. Both increase the skewness of the elements, forcing the Jacobian of some finite elements to be close to zero and consequently the global Jacobian matrix to be nearly singular. In order to overcome this, the mesh is reconstructed when it is considered necessary, i.e. before the elements become overly skewed. The need to reconstruct the mesh is signalled by the increase or decrease beyond a certain limit of the number of elements around the two bubbles, depending on the case. During the whole simulation, the results are accurate and mesh-independent in contrast to Eulerian-type methods (e.g. level set). For the solution of the linear algebraic systems of equations that arise at each time step after the Newton–Rapshon linearization, we have used a message passing interface (MPI) – parallel library based on multilevel incomplete LU decomposition (ILU) pre-conditioner (Hènon & Saad 2006; Gaidamour & Hènon 2008).

4. Results

4.1. *Normal-mode analysis*

Before proceeding with the nonlinear dynamics and in order to interpret and classify the numerical predictions, it is imperative to perform a normal-mode analysis of the two deformable bubbles interacting in a Newtonian liquid. This will determine the frequencies and the damping rates of the system under small disturbances. Such data have not been reported before because even these linearized equations do not seem to be amenable to analytical treatment. Nevertheless, these data can be extracted with our numerical code by assuming that initially no flow exists and the two bubbles are spherical due to capillarity and, then, subjecting all the flow variables including the bubble shapes to an infinitesimal disturbance. More specifically, the normal modes of the system are computed by assuming that all variables are split into their base (static equilibrium) values and a small disturbance:

$$\begin{bmatrix} \boldsymbol{u}(r,\theta,t) \\ P(r,\theta,t) \\ P_g(r,\theta,t) \\ \boldsymbol{x}(r,\theta,t) \end{bmatrix} = \begin{bmatrix} \boldsymbol{u}_b \\ P_b \\ P_{gb} \\ \boldsymbol{x}_b \end{bmatrix} + \delta \begin{bmatrix} \boldsymbol{u}_p(r,\theta) \\ P_p(r,\theta) \\ P_{gp}(r,\theta) \\ \boldsymbol{x}_p(r,\theta) \end{bmatrix} \mathrm{e}^{ct}. \tag{4.1}$$

Here, the new subscripts b and p indicate the equilibrium and the perturbed states, respectively, $\delta \ll 1$ is the amplitude of the infinitesimal disturbance, and $\boldsymbol{x}$ denotes the position vector of the mesh nodes including the nodes at the interfaces of the bubbles. Hence, $\boldsymbol{u}_b = 0$, P_b equals the hydrostatic pressure in the liquid and P_{gb}, the bubble basic pressure, which is set by capillarity with respect to P_b. Substituting expressions (4.1) into the governing equations, including the kinematic equation (2.7) and the equation of state (2.9), and neglecting terms of order higher than linear in the perturbation parameter, δ, we obtain a generalized eigenvalue problem of the form

$$\boldsymbol{JY} = c\boldsymbol{MY}, \tag{4.2}$$

where $\boldsymbol{J}$ is the Jacobian matrix, $\boldsymbol{M}$ is the mass matrix, c are the eigenvalues, and $\boldsymbol{Y}$ are the corresponding eigenvectors. In order to solve the eigenvalue problem, we used

https://doi.org/10.1017/S0022112010006361 Published online by Cambridge University Press

the Arnoldi method as it is implemented in the Arpack library (Lehoucq, Sorensen & Young 1998).

On the other hand, analytical results of the simpler normal-mode analysis for an isolated bubble in a Newtonian liquid have been reported in the literature. Comparing our numerical predictions for the computed eigenfrequencies in the limit of large distance between the bubble centres in comparison with their radii to the analytical expressions for a single bubble provides a strict and demanding test for the accuracy of our numerical simulations and an indication for the extent to which the computational mesh must be refined. In particular, assuming that (i) the surrounding liquid is incompressible, (ii) thermal effects are negligible, (iii) the interface has no elasticity or intrinsic viscosity, and that the bubble undergoes only radial oscillations, yields the classical Rayleigh–Plesset equation (Plesset & Prosperetti 1977; Brennen 1995; Tsiglifis & Pelekasis 2007). Further assuming that the disturbance amplitude is small and using the scales for the variables employed herein reduces it to the linearized equation

$$R_p'' + 4\ Oh\ R_p' + \{3\gamma\,(P_b + 2) - 2\}\,R_p = 0, \tag{4.3}$$

where the primes indicate differentiation with respect to time. The roots of its characteristic polynomial furnish the eigenvalue of (4.3), $c_{o,\infty} = -\beta_{o,\infty} \pm \mathrm{i}\omega_{o,\infty}$, written in terms of the dimensionless resonance frequency, $\omega_{o,\infty}$ (or the oscillation period, $T_{o,\infty}$) and damping, $\beta_{o,\infty}$, of the isolated bubble:

$$T_{o,\infty} = \frac{2\pi}{\omega_{o,\infty}} = \frac{2\pi}{[3\gamma\,(P_b + 2) - 2 - 4\ Oh^2]^{1/2}} = \frac{2\pi}{\left[3\gamma\left(\dfrac{P_b^*}{\sigma^*/R_b^*} + 2\right) - 2 - \dfrac{4\mu^{*2}}{\rho^*\sigma^* R_b^*}\right]^{1/2}},$$
$$\beta_{o,\infty} = 2\ Oh. \tag{4.4}$$

The subscript 'o' indicates that the corresponding variables refer to the mode preserving spherical symmetry, often called the breathing or the zeroth mode, while the subscript ∞ indicates that the bubble is isolated. These expressions demonstrate that the dimensionless damping rate is proportional to Oh, while the period decreases with the dimensionless ambient pressure (scaled with capillarity), but increases with the Ohnesorge number approximately as $P^{-1/2}$ and Oh, respectively, when each one of them dominates the rest of the terms in the denominator of (4.4) or that the period increases when the liquid viscosity increases and it decreases when the bubble radius increases.

The corresponding eigenmode analysis which allows even for deformations of the bubble surface is quite more involved. Miller & Scriven (1968) have examined the more general problem of a deformable spherical globule composed of a Newtonian fluid and immersed in another immiscible fluid which extends to infinity. They have shown that the vorticity and the radial velocity of the linearized equations may be expressed in terms of spherical harmonics and generalized radial functions, and provided expressions to determine the eigenvalues of the system. In the limit of inner to outer fluid density and viscosity ratios approaching zero, the problem of an isolated bubble is recovered. In this case, the dimensional eigenvalues $c_{l,\infty}^*$ are given by the following closed-form but implicit expression:

$$\frac{\omega_{inv}^{*2}}{c_{l,\infty}^{*2}} = \frac{l+2}{\omega^{*2}R_b^{*2}}\left[\frac{(2l+1)\omega^{*2}R_b^{*2} - 2(l-1)(l+1)\left(2l+1-\omega^* R_b^* Q_{l+(1/2)}^H\right)}{2l+1-\omega^* R_b^* Q_{l+(1/2)}^H + \omega^{*2}R_b^{*2}/2}\right] - 1,$$
$$l = 2, 3, \ldots, \tag{4.5a}$$

https://doi.org/10.1017/S0022112010006361 Published online by Cambridge University Press

where $\omega^* = \sqrt{c^*_{l,\infty}\rho^*/\mu^*}$ has units of inverse length, is related to the eigenvalue $c^*_{l,\infty}$ and is introduced only for convenience, while $\omega^*_{inv} = \{[\sigma^*(l+1)(l-1)(l+2)]/R^{*3}_b\rho^*\}^{1/2}$ is the frequency of oscillation, if the surrounding liquid is assumed to be inviscid and the gas in the bubble does not contribute to the dynamics of the problem (see Rayleigh 1917; Tsamopoulos & Brown 1983). Finally,

$$Q^H_{l+(1/2)} \equiv \frac{H^{(1)}_{l+(3/2)}(\omega^* R^*_b)}{H^{(1)}_{l+(1/2)}(\omega^* R^*_b)}, \tag{4.5b}$$

where $H^{(1)}_{l+(1/2)}$ and $H^{(1)}_{l+(3/2)}$ are the half-integral-order Hankel functions of the first kind. In these expressions, l corresponds to the index of the Legendre polynomial characterizing the shape of the bubble. The analytical solution does not apply to volume oscillations of the bubble ($l=0$) or bubble translation ($l=1$). Here again, writing $c_{l,\infty} = -\beta_{l,\infty} \pm \mathrm{i}\omega_{l,\infty}$, one obtains the decay factor as the real part of $c_{l,\infty}$, while its imaginary part is the angular frequency of the lth mode.

Next, the oscillation frequencies and decay factors computed numerically with our code are compared with their values calculated by solving (4.5a) using standard software for the $l \geqslant 2$ modes and directly from (4.4) for the $l=0$ mode. Typically, properties of pure water at an ambient temperature of 20°C and pressure 1 bar are used, i.e. $\rho^* = 10^3\,\mathrm{kg\,m^{-3}}$, $\mu^* = 10^{-3}\,\mathrm{Ns\,m^{-2}}$, $\sigma^* = 0.0727\,\mathrm{N\,m^{-1}}$. When these are combined with the bubble size, they yield the particular Ohnesorge number and dimensionless pressure. Table 1(a) gives the dimensionless eigenvalues obtained for two equal bubbles with $R^*_b = 5\,\mu\mathrm{m}$ in water; hence, $Oh^{-1} = 19.065$, $P = 6.878$, located at a large distance $D = 17$, where it is anticipated that the bubbles will not interact, at least in the linear limit. Indeed, two identical sets of eigenvalues result for each wavenumber, each set corresponding to each one of the bubbles. The eigenvalues obtained with the increased spatial discretization of the meshes M3, M4 and M5 monotonically approach their values calculated using the analytical expressions of (4.4) and (4.5a). This confirms that in spite of the large distance between the bubbles which increases the distance between the nodes in the computational mesh, the numerical values are highly accurate even with the coarsest mesh. The characteristics of the mesh are given in table 1(d). In general, the eigenvalues have converged to at least 2–3 digits with the M3 mesh and to 3–4 digits with the M5 mesh.

The eigenfrequencies of the same bubbles when they are closer together at $D = 2.8$ or 5 are given in table 1(b,c). The smaller distance between the two bubbles increases the local refinement around each bubble and, hence, improves the convergence of the eigenvalues to 4–5 digits typically even with less refined mesh. Therefore, for these two smaller interbubble distances, discretization even with the M3 mesh is more than sufficient in the dynamic simulations that will follow. This mesh will be used in the bulk of the remaining calculations. Now, two different sets of eigenvalues arise for each wavenumber, the one with smaller real and imaginary parts corresponding to in-phase oscillations of the bubbles and the larger one to out-of-phase oscillations. This difference in the two eigenvalues is larger for the lower modes of oscillation. For the zeroth mode, in-phase oscillations arise when the two bubbles expand and contract simultaneously, whereas out-of-phase oscillations arise when one of the bubbles expands while the other one contracts. For the second mode, in-phase oscillations arise when both bubbles assume the prolate shape (extended along the axis of symmetry) and then the oblate shape (flattened at their poles) simultaneously, while out-of-phase oscillations arise when one bubble assumes the prolate shape while the other assumes the oblate shape. A similar differentiation of the eigenvalues was obtained

https://doi.org/10.1017/S0022112010006361 Published online by Cambridge University Press

https://doi.org/10.1017/S0022112010006361 Published online by Cambridge University Press

(*a*) $D = 17$ (nearly isolated bubbles)

l	For $l = 0$ from (4.4), for $l \geqslant 2$ from (4.5*a*)	M3	M4	M5
0	-0.1049 ± 5.9394i	-0.1057 ± 5.9641i	-0.1055 ± 5.9640i	-0.1055 ± 5.9639i
2	-0.7533 ± 3.2030i	-0.7568 ± 3.2858i	-0.7551 ± 3.2447i	-0.7543 ± 3.2268i
3	-1.3166 ± 5.8695i	-1.3192 ± 5.9312i	-1.3179 ± 5.9004i	-1.3173 ± 5.8871i
4	-2.0104 ± 8.7725i	-2.0128 ± 8.8243i	-2.0116 ± 8.7984i	-2.0111 ± 8.7872i
5	-2.8326 ± 11.9223i	-2.8349 ± 11.9681i	-2.8337 ± 11.9452i	-2.8332 ± 11.9354i

(*b*) $D = 5$

l	c_l (in-phase)			c_l (out-of-phase)		
	M3	M4	M5	M3	M4	M5
0	-0.09316 ± 5.57261i	-0.09312 ± 5.57260i	-0.093126 ± 5.57259i	-0.13295 ± 6.6249i	-0.13293 ± 6.62489i	-0.13292 ± 6.62488i
2	-0.752958 ± 3.19809i	-0.752952 ± 3.19808i	-0.752950 ± 3.19807i	-0.753699 ± 3.20847i	-0.753693 ± 3.20846i	-0.753691 ± 3.20845i
3	-1.31659 ± 5.86827i	-1.31658 ± 5.86826i	-1.31657 ± 5.86825i	-1.31664 ± 5.8709i	-1.31663 ± 5.87089i	-1.31662 ± 5.87088i
4	-2.01048 ± 8.77222i	-2.01043 ± 8.77219i	-2.01042 ± 8.77218i	-2.01048 ± 8.77278i	-2.01044 ± 8.77275i	-2.01043 ± 8.77274i
5	-2.8327 ± 11.9225i	-2.8326 ± 11.9224i	-2.83257 ± 11.9223i	-2.8326 ± 11.9226i	-2.83259 ± 11.9225i	-2.83258 ± 11.9224i

(*c*) $D = 2.8$

l	c_l (in-phase)			c_l (out-of-phase)		
	M3	M4	M5	M3	M4	M5
0	-0.08763 ± 5.17987i	-0.08762 ± 5.17987i	-0.08761 ± 5.17987i	-0.179 ± 7.1377i	-0.17897 ± 7.1377i	-0.17895 ± 7.1377i
2	-0.74939 ± 3.12178i	-0.74938 ± 3.12177i	-0.74937 ± 3.12176i	-0.76495 ± 3.30662i	-0.76494 ± 3.30661i	-0.76493 ± 3.3066i
3	-1.31604 ± 5.80397i	-1.31602 ± 5.80396i	-1.31601 ± 5.80395i	-1.31916 ± 5.94968i	-1.31914 ± 5.94967i	-1.31913 ± 5.94966i
4	-2.00989 ± 8.72786i	-2.00983 ± 8.72783i	-2.00981 ± 8.72782i	-2.0112 ± 8.82386i	-2.01118 ± 8.82382i	-2.01117 ± 8.82381i
5	-2.8315 ± 11.8943i	-2.83137 ± 11.8944i	-2.83133 ± 11.8942i	-2.8338 ± 11.9533i	-2.83368 ± 11.9532i	-2.83365 ± 11.9531i

(*d*) Characteristics of the three meshes used

Mesh	Total number of triangles after local refinement	Number of nodes on each free surface after refinement	Δr_{min} around the free surface after local refinement	Δz_{min} around the free surface after local refinement
M3	15 360	641	0.01	0.002
M4	30 720	1281	0.005	0.002
M5	53 760	2241	0.003	0.002

TABLE 1. Eigenvalues for two bubbles of equal radii $R_b^* = 5\,\mu$m, immersed in pure water at ambient temperature $T^* = 20^\circ$C and pressure $P^* = 1$ bar; hence $Oh^{-1} = 19.065$ and $P = 6.878$ for three different interbubble distances: (*a*) $D = 17$, (*b*) $D = 5$ and (*c*) $D = 2.8$. In table 1(*d*) we give the characteristics of the three meshes that are used.

Case	R^*_{bi}	D	ε	$T_{0,\infty}$ based on P	$T_{0,\infty}$ based on $P(1+\varepsilon)$	$T_{0,\infty}$ based on algorithm	$R_{b.eq}/R_b$
1	5 μm	2.8	1	1.057	0.676	0.762	0.868
2	10 μm	2.8	1	0.784	0.479	0.541	0.859
3	20 μm	2.8	1	0.569	0.347	0.393	0.854
4	30 μm	2.8	1	0.468	0.284	0.333	0.852
5	30 μm	5	1	0.468	0.284	0.309	0.852
6	40 μm	2.8	1	0.407	0.247	0.285	0.851
7	40 μm	2.8	0.2	0.407	0.357	0.409	0.958
8	100 μm	5	1	0.260	0.156	0.168	0.849
9	1 mm	2.8	1	0.082	0.049	0.058	0.848
10	1 mm	2.8	0.3	0.082	0.068	0.078	0.939
11	1 mm	5	1	0.082	0.049	0.053	0.848
12	1 mm	9.9	1	0.082	0.049	0.051	0.848
13	1 mm	9.9	0.3	0.082	0.068	0.069	0.939

TABLE 2. The period of the breathing mode calculated from (4.4) either with the initial hydrostatic pressure P or after imposing the step increase in pressure $P(1+\varepsilon)$. The first period of volume oscillations resulting from the present algorithm and the ratio of the equilibrium to the initial bubble radius are also given.

in Pelekasis & Tsamopoulos (1993*a*), where the liquid surrounding the two bubbles was assumed to be inviscid and a much larger dimensionless hydrostatic pressure was used, resulting in larger eigenvalues of the zeroth mode. In Newtonian liquids as well, we find that as D decreases, both parts of the eigenvalue corresponding to in-phase oscillations decrease, while those corresponding to out-of-phase oscillations increase. Physically, one may explain this by noting that in the first case, during their simultaneous expansion, the bubbles interfere with each other, decreasing their eigenfrequency, whereas in the second case the expansion of one bubble promotes the contraction of the other bubble, increasing their frequency. This is demonstrated here by comparing in table 1 the eigenvalues for $D = 2.8$, 5 and 17, where we see that in smaller distances the deviation between the two sets of eigenvalues is clear, in the intermediate distance it occurs in the third or fourth significant digit of the eigenvalues, whereas there is no deviation in the largest distance.

4.2. *Nonlinear dynamics of equal bubbles*

The code used for the stability analysis is modified to perform nonlinear simulations of two interacting bubbles for a wide range of radii (1 μm–1 mm) immersed in pure water, when the ambient pressure increases from 1 bar by up to 100 %. Hence, the disturbance amplitude, ε, in the following simulations, except for those in § 4.2.4, where the effect of ε is examined, is set to $\varepsilon = 1$. Among the several cases that we have examined, the discussion that follows is focused on those cases listed in table 2. Although these exhibit very different bubble dynamics and shape deformations, they will help us extract certain common features related to the secondary Bjerknes force.

4.2.1. *Bubbles with* $R^*_b = 5\,\mu\text{m}$ *and* $D^* = 14\,\mu\text{m}$ *and general characteristics of the motion*

First, two equal bubbles of a relatively small radius, 5 μm, are examined, when immersed in pure water. Therefore, for this case the pressure at the far field is increased at $t = 0$ to $P_\infty = P(1+\varepsilon) = 13.756$. The initial distance between the centres of volume of the two bubbles is set to $D = 2.8$. Figure 2 shows the time variation

https://doi.org/10.1017/S0022112010006361 Published online by Cambridge University Press

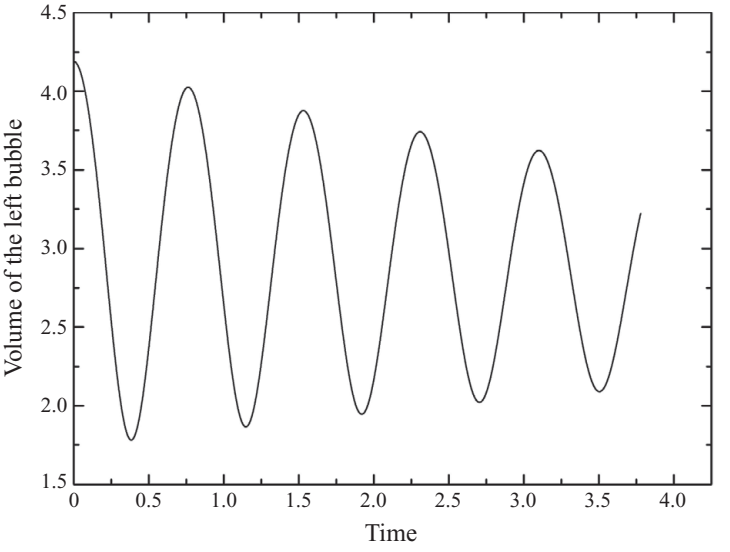

FIGURE 2. Variation with time of the volume of the left bubble. The two bubbles are equal with $R_b^* = 5\,\mu\text{m}$, $Oh^{-1} = 19.065$, $P = 6.878$ and $D = 2.8$.

of the dimensionless volume of the left bubble, which initially is $V = 4\pi/3 = 4.1888$. Doubling of the far-field pressure quickly reduces the bubble volume below its new equilibrium value, $V_{eq} = 2.742$, and even to less than half its initial size, $V \approx 1.75$. Subsequently, the bubble undergoes damped oscillations because of fluid viscosity. The volume of the right bubble varies with time in exactly the same way owing to symmetry. Oscillations of the two bubbles are in-phase and their first common period is found to be $T_0 = 0.762$, and subsequent periods of volume oscillations slowly increase with time: 0.768, 0.778 and 0.792. All these are lower than the value predicted by the normal-mode analysis for in-phase volume oscillations for $P = 6.878$, which according to (4.4) gives $T_{o,\infty} = 1.057$. This decrease in the period of the nonlinear oscillations is because the zeroth mode that corresponds to the volume oscillations is mainly affected by changes in dimensionless pressure. The large pressure increase leads to a new equilibrium bubble radius of 0.868, resulting in a linear period of 0.676 (see table 2). This value is slightly smaller than the numerically calculated one because nonlinear effects increase the importance of inertia and hence the period of bubble oscillations (see Tsamopoulos & Brown 1983).

Figure 3 shows the evolution of the centres of volume of each bubble with time, for the present and some other cases to be discussed subsequently. Their locations, Z_i, for each bubble, i, are determined along their common axis of symmetry via

$$Z_i = \frac{\iiint_V z\,\mathrm{d}V}{\iiint_V \mathrm{d}V} = \frac{\int z\rho(z)^2\,\mathrm{d}z}{\int \rho(z)^2\,\mathrm{d}z} = \frac{\int z\rho(z)^2 \dfrac{\mathrm{d}z}{\mathrm{d}s}\,\mathrm{d}s}{\int \rho(z)^2 \dfrac{\mathrm{d}z}{\mathrm{d}s}\,\mathrm{d}s}, \quad i = 1, 2, \tag{4.6a}$$

where cylindrical coordinates (z, ρ) have been introduced, which are centred at their common axis. In the third ratio of integrals, the integration with respect to the axial distance has been transformed into integration with respect to the arclength, s, along the bubble surface to avoid the multi-valuedness of some bubble shapes, as we will

https://doi.org/10.1017/S0022112010006361 Published online by Cambridge University Press

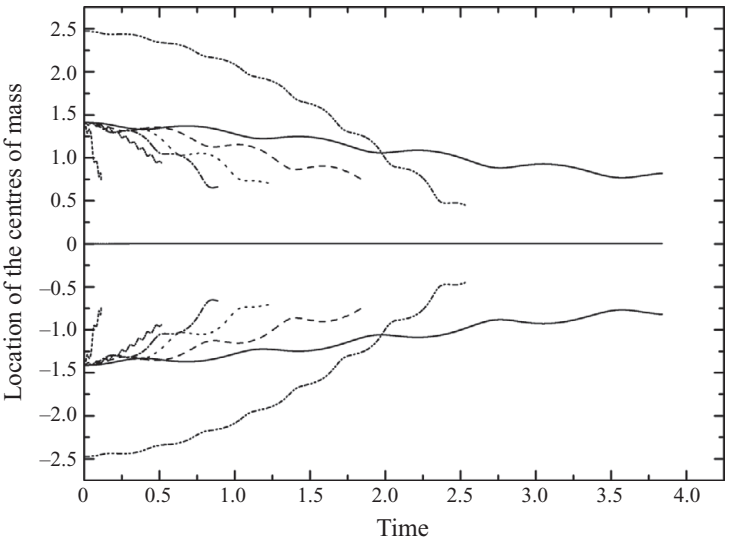

FIGURE 3. Evolution of the centres of volume of the two equal bubbles with (—) $R_b^* = 5\,\mu$m, $D = 2.8$, $\varepsilon = 1$; (——) $R_b^* = 10\,\mu$m, $D = 2.8$, $\varepsilon = 1$; (· · · · · ·) $R_b^* = 20\,\mu$m, $D = 2.8$, $\varepsilon = 1$; (–·–) $R_b^* = 30\,\mu$m, $D = 2.8$, $\varepsilon = 1$; (—··—) $R_b^* = 30\,\mu$m, $D = 5$, $\varepsilon = 1$; (- -) $R_b^* = 40\,\mu$m, $D = 2.8$, $\varepsilon = 1$; (-··-) $R_b^* = 40\,\mu$m, $D = 2.8$, $\varepsilon = 0.2$.

see in the next sections. The combined centre of volume Z is computed via

$$Z = \frac{Z_1 V_1 + Z_2 V_2}{V_1 + V_2}. \tag{4.6b}$$

The two centres of volume are seen to oscillate symmetrically and keep approaching each other in a slower time scale. The combined centre of volume remains at zero owing to the plane of symmetry, verifying once again the accuracy of our calculations. The final distance between the bubble centres is ∼1.55, i.e. less than the sum of the current bubble radii, which is ∼1.85. This reveals that the bubbles have approached each other so much that they have squeezed each other, attaining a deformed oblate shape. Bubble pairs flattened on the portion of their interfaces facing each other when they get close together and just before coalescence have been observed experimentally (e.g. Lauterborn *et al.* 1999). Calculating the average distance between the bubble centres within each oscillation period and fitting these data to a quadratic polynomial in time, one obtains

$$D_{average} = 2.804 - 0.186\,t - 0.06\,t^2. \tag{4.7}$$

This time-dependence shows that the bubbles accelerate towards each other on average.

In figure 4(a, b), the velocity and acceleration, respectively, of the centre of the left bubble are shown and are also oscillatory. These are determined by numerically differentiating with respect to time the instantaneous locations of the bubble centres. This figure and figures 2 and 3 are given up to $t = 3.778$, when the bubble surfaces are too close to each other as shown next. The average velocity over a period of volume oscillations initially increases with time almost linearly, then it increases at a lower rate and, finally, decreases at the last stages of the simulations and after the two bubbles have approached each other significantly. Apparently, the two bubbles have come so close together that their translation along their common axis cannot continue.

https://doi.org/10.1017/S0022112010006361 Published online by Cambridge University Press

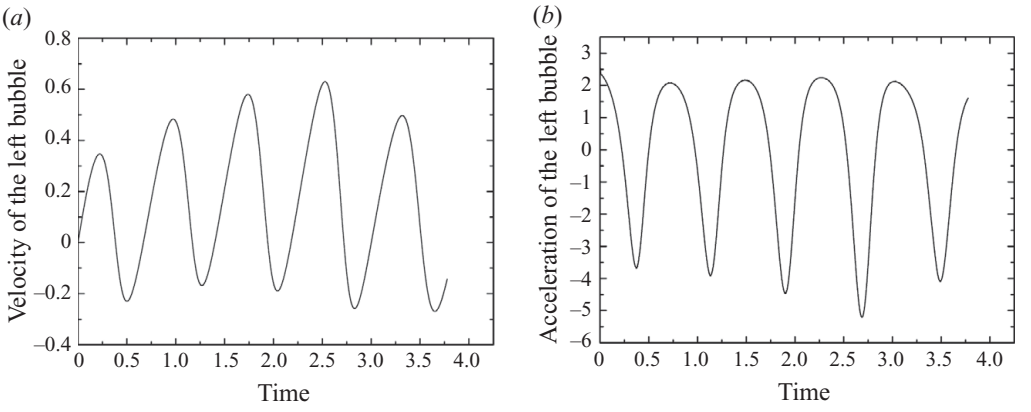

FIGURE 4. Evolution with time of (*a*) the velocity and (*b*) the acceleration of the left bubble. The two bubbles are equal with parameters as in figure 2.

Figure 4(*b*) shows that the left bubble spends more time accelerating towards the right one than decelerating away from it. The values of the average acceleration over each period of volume oscillation are $\langle g \rangle = 0.248$, 0.099, 0.007, 0.089 and remain always positive, so that the average force remains attractive until the end of the simulation. Because of this strong time-dependence of the bubble acceleration, in all calculations determining the secondary Bjerknes force that follow the average acceleration of the bubbles will be measured and reported on the first period of volume oscillations. This seems to be most appropriate since the bubbles deform and approach each other with time, both of which affect their acceleration. The oscillation periods of the velocity and the acceleration slowly increase, following the same trend of the periods in the volume oscillations. Only the last figure signals a decrease in the amplitude just because the two bubbles are now very close and prevent each other from accelerating further. This increase in the periods is attributed to the slow viscous damping of the nonlinear oscillations (Nayfeh & Mook 1979).

Figure 5 presents the bubble shapes and contour plots of both velocity components and pressure at $t = 3.148$. At this instant, the bubbles have approached each other significantly, as their nearby surfaces are at a distance of 0.039 or 0.195 μm. This distance still allows us to neglect van der Waals and other surface forces or merging of the bubbles. The field variables are presented with respect to a spherical coordinate system centred at the middle of the distance between the initial centroids of the two bubbles. The radial velocity, given in the upper half of figure 5(*a*), takes its smallest (negative) values at the rear side of the bubbles, while it takes positive values between the two bubbles. This distribution of v_r indicates that the two bubbles are in the contracting phase of their radial oscillation but still approach each other, squeezing fluid away from the gap between them. The former can be confirmed by observing in figure 2 that the time $t = 3.148$ is just after the last maximum in the volume oscillations of the bubbles, indicating that they have started their final contraction. The azimuthal velocity, given in the lower half of figure 5(*a*), is symmetric with respect to $\theta = \pi/2$, because the two bubbles are equal and undergo in-phase oscillations, producing a plane of symmetry normal to their common axis. As the two bubbles contract, the azimuthal velocity takes negative values around the left bubble and positive values around the right bubble, while it is zero at $\theta = 0$ and $\theta = \pi$, due to axial symmetry. The pressure field, which is given in figure 5(*b*), forms contours surrounding both

https://doi.org/10.1017/S0022112010006361 Published online by Cambridge University Press

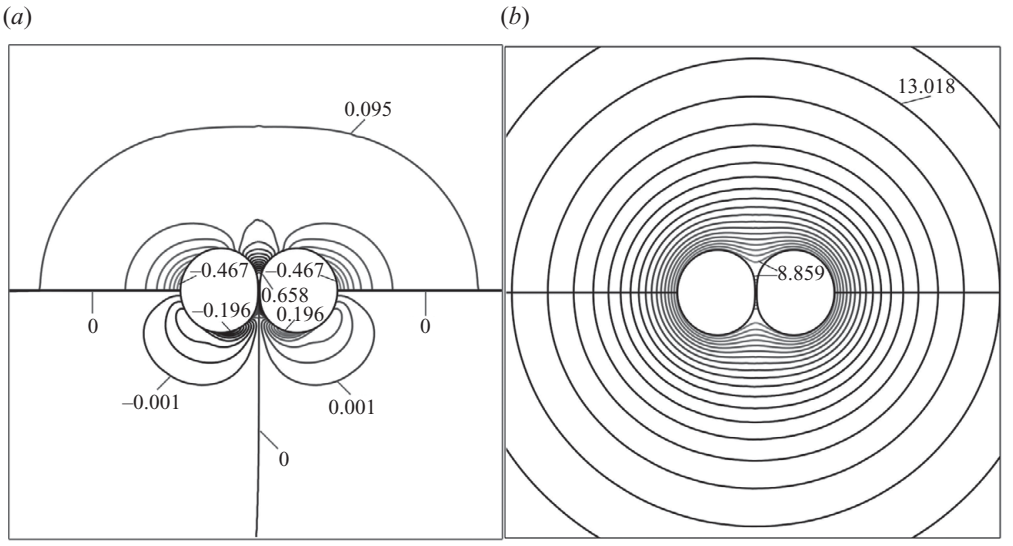

FIGURE 5. Contours of (*a*) u_r (upper half), u_θ (lower half) and (*b*) P at $t = 3.73$ for $R_b^* = 5\,\mu\text{m}$, $Oh^{-1} = 19.065$, $P = 6.67$, $\varepsilon = 1$ and $D = 2.8$. The range of the respective variable is divided into 20 equal intervals.

bubbles very close to them. Apparently, the bubbles, being in their contraction phase, have overshot their new equilibrium position and the pressure near their surface is well below than that imposed in the outer boundary. Indeed, the pressure just outside the bubbles is 8.859. At a distance less than 7 bubble radii from the centre of this coordinate system, the pressure attains radial symmetry. Moreover, the pressure, which has been set at $P_\infty = P(1+\varepsilon) = 13.756$ at $R_\infty = 30$, decreases only to $P = 13.018$ very close to the bubble, at a distance of approximately $r \approx 5$ in this coordinate system, which verifies once more that locating the outer boundary at $R_\infty = 30$ does not affect even the pressure field, which is the most sensitive of the flow variables.

The Fourier–Legendre decomposition of the bubble shape helps in determining the detailed dynamics of the interacting bubbles. The Fourier–Legendre coefficients are computed with respect to spherical coordinates with origin located at the instantaneous centre of each bubble and are given by

$$C_l = \int_0^\pi f_s(\theta) P_l(\theta) \sin(\theta)\, \mathrm{d}\theta, \quad l = 0, 1, 2, 3 \ldots . \tag{4.8}$$

Since the bubbles are equal and oscillate in-phase, the normal-mode decomposition of their interface is identical. The amplitude of the zeroth mode undergoes damped oscillations in exact correspondence to the volume oscillations reported in figure 2. Figure 6 shows the time evolution of the coefficient C_2 of the second Legendre polynomial P_2, of the left bubble for this and some cases to follow. Positive values of the coefficient C_2 signify prolate bubble shapes (elongated along the axis of symmetry), whereas negative values signify oblate bubble shapes (flattened at the bubble poles). Both bubbles oscillate, initially attaining alternatively prolate and oblate shapes, but eventually they attain only oblate shapes because they have squeezed each other along their common axis. Although the two bubbles have approached each other considerably, as can be seen in figure 5, they did not flatten significantly, because of their very small size which makes capillary forces dominant over all other forces, as

https://doi.org/10.1017/S0022112010006361 Published online by Cambridge University Press

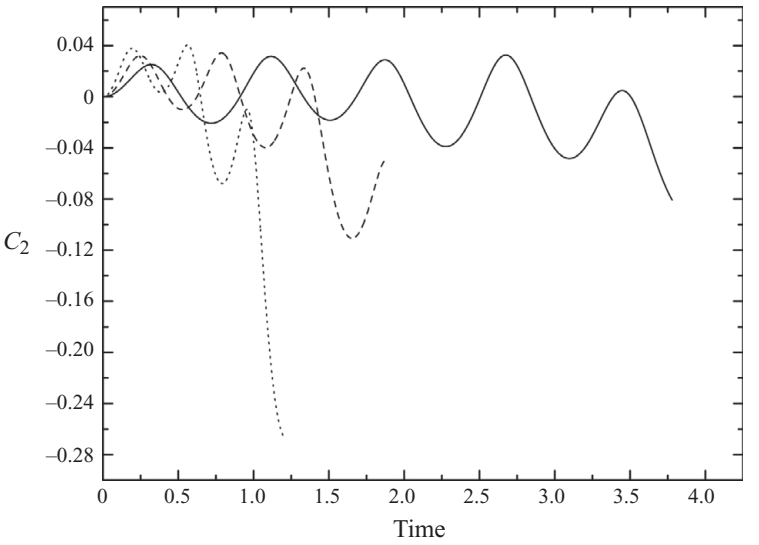

FIGURE 6. Time evolution of the C_2 coefficient of the Fourier–Legendre decomposition of the bubble surface. The two bubbles are equal with (—) $R_b^* = 5\,\mu$m, (--) $R_b^* = 10\,\mu$m and (· · · · · ·) $R_b^* = 20\,\mu$m.

indicated by the small value of Oh^{-1}. For the same reason, all modes higher than P_2 have negligible contribution to the bubble shape.

4.2.2. *Effect of bubble size when they are close to each other*

Retaining the initial dimensionless distance between the two bubbles at $D = 2.8$, we increased the bubble radius from 5 to 10 μm ($Oh^{-1} = 26.962$, $P = 13.755$) and then to 20 μm ($Oh^{-1} = 38.131$, $P = 27.51$). As seen in table 2, the dimensionless period of volume oscillations decreases as the bubble radii increase irrespective of whether it is calculated based on the initial pressure or after imposing the step increase in pressure, both from (4.4) or from the present algorithm. One may easily verify that the discussion that follows is not affected in any way, if one chooses to calculate the eigenfrequencies with the equilibrium bubble radius prior or after applying the step change in pressure. As expected, this variation in the oscillation period with the bubble radius is reversed when the time scale we employed, $(R_b^{*3}\rho^*/\sigma^*)^{1/2}$, is accounted for to obtain the dimensional period. Because of the smaller period of volume oscillations and larger bubble volumes, it is expected that the average acceleration of the bubbles will increase with their size and, consequently, the dimensionless time needed to approach each other will decrease. Indeed, from figure 3, where the locations of the centres of volume for the present two cases are given as well, it is obvious that the larger the bubbles, the less time is needed to approach each other. Again, we can calculate the average distance between the two bubble centres within each oscillation period and fit these data to a quadratic polynomial in time. For $R_b^* = 10\,\mu$m, this yields

$$D_{average} = 2.778 - 0.222\,t - 0.308\,t^2. \tag{4.9}$$

As for the $R_b^* = 5\,\mu$m case, this expression gives approximately the initial interbubble distance and the average acceleration, which here is 0.616, i.e. much larger than in bubbles with $R_b^* = 5\,\mu$m. In figure 3, we can also see that the final distance between the bubble centres is smaller than the sum of their current radii and somewhat smaller than for the 5 μm bubbles.

https://doi.org/10.1017/S0022112010006361 Published online by Cambridge University Press

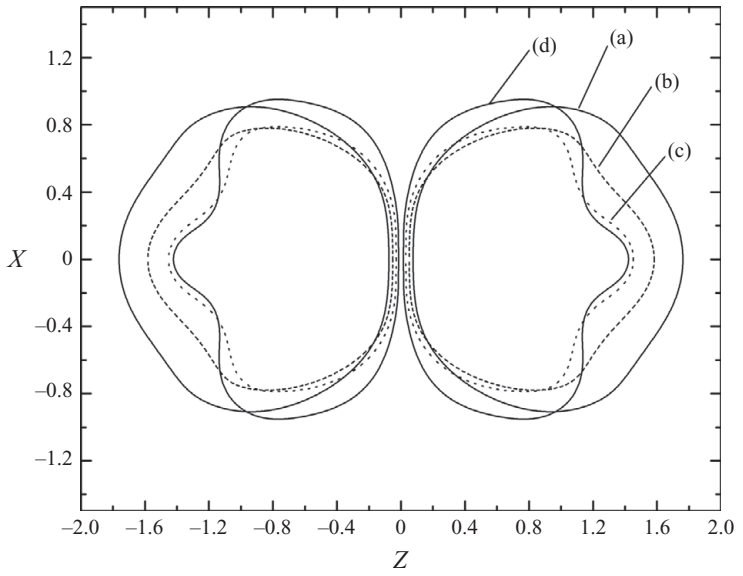

FIGURE 7. Bubble shapes at (a) $t = 0.738$, (b) $t = 0.788$, (c) $t = 0.837$ and (d) $t = 0.886$ for two equal bubbles with $R_b^* = 30\,\mu\text{m}$, $Oh^{-1} = 46.701$, $P = 41.265$, $\varepsilon = 1$ and $D = 2.8$.

The time evolution of the zeroth, C_0, coefficients of the Legendre polynomials, P_0, for these two radii, are available in Chatzidai (2008). They also demonstrate that the period of the volume oscillations decreases when the size of the bubble increases, while the amplitude of the oscillations increases. The former results from the increased dimensionless pressure, while the latter results from the increased inertia. The deformations of the bubble surfaces are expected to be larger, since the increased Oh^{-1} signifies less important capillary forces with respect to viscous forces. Coupling this effect with the increased average acceleration when the bubble size increases leads to the anticipation that the larger bubbles will attain more flattened shapes. Indeed, comparing the values of C_2 in figure 6 for the bubbles of 5, 10 and 20 μm, it is clear that the shape of the larger bubble is characterized by a more negative coefficient towards the end of the simulations, which signals a flatter bubble. Comparing the oscillation periods of the zeroth 0.541, 0.548, 0.562 and the second modes 0.528, 0.552, 0.574, for example, for the $R_b^* = 10\,\mu\text{m}$ bubbles, we find not only that they both increase in time but, more importantly, that the periods of these two modes are similar. It is noteworthy that the linear period of P_2 is 1.901 (or 1.397 when the decreased equilibrium radius is accounted for), i.e. very different from the periods of the computed modes. This implies that the bubbles are deformed not because of a harmonic or subharmonic resonance of the second mode, but because of their volume oscillation and their squeezing each other.

Increasing the bubble radius even more to 30 μm ($Oh^{-1} = 46.701$, $P = 41.265$), modes higher than P_2 start to arise and the two bubbles deform on the side facing away from the direction of average acceleration. Hereafter, this side will be called the rear side, while the other side will be called the front side. Figure 7 gives a sequence of bubble shapes at the same initial interbubble distance up to the instant that the bubble front surfaces are too close to each other. The Fourier–Legendre decomposition of these shapes is given in figure 8 for the coefficients of P_2–P_6. Among the surface harmonics, the second harmonic is seen to start growing immediately with

https://doi.org/10.1017/S0022112010006361 Published online by Cambridge University Press

l	c_l (in-phase)	c_l (out-of-phase)	T_l
0	-0.0357 ± 11.6850i	-0.0764 ± 16.0745i	0.332
2	-0.3500 ± 3.3078i	-0.3584 ± 3.5035i	0.29
3	-0.6158 ± 6.1316i	-0.6189 ± 6.2859i	0.5
4	-0.9471 ± 9.2444i	-0.9480 ± 9.3470i	0.437
5	-1.3436 ± 12.6470i	-1.3436 ± 12.7104i	0.421
6	-1.8045 ± 16.3220i	-1.8047 ± 16.3598i	0.418

TABLE 3. Eigenvalues c_l and first periods of the nonlinear oscillations T_l for equal bubbles with $R_b^* = 30\,\mu$m, $Oh^{-1} = 46.701$, $P = 41.265$ and $D = 2.8$.

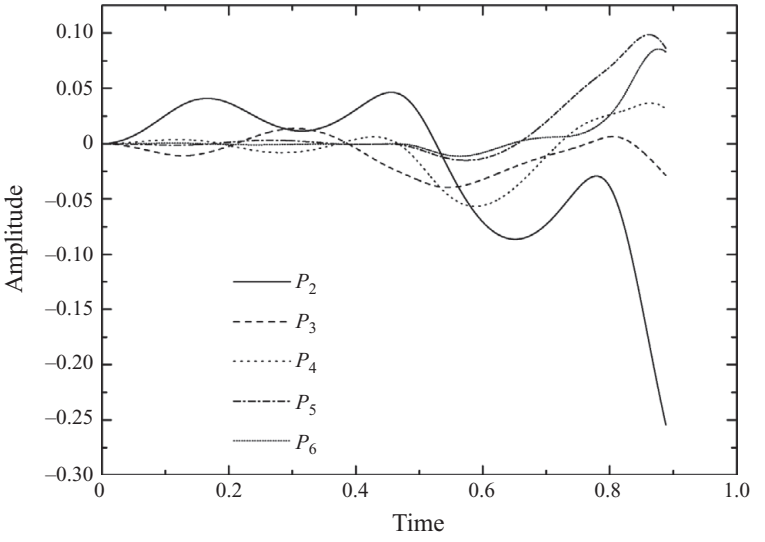

FIGURE 8. Time evolution of the coefficients c_2–c_6 of the Fourier–Legendre decomposition of the bubble surface for two equal bubbles with the parameters as in figure 7.

approximately the same period as the zeroth mode, followed by the third one, then the rest of the higher modes follow. Towards the end of the simulations, the second harmonic has the largest amplitude, which has even approached the amplitude of the zeroth mode, followed by the fifth and sixth modes. Table 3 presents the eigenvalues of the breathing mode and the P_2–P_6 modes calculated using (4.4) and (4.5*a*) respectively. The table also presents the corresponding nonlinear periods of the first oscillation as computed by our finite element algorithm. We observe that the computed frequency of the P_3 mode is almost half the frequency of the in-phase breathing mode, while the frequencies of the P_5 and P_6 modes are close to its value. This indicates a shape deformation not observed above with smaller bubbles, but arising through the so-called parametric resonance, first discussed by Plesset (1954), for a single bubble. Later, Hall & Seminara 1980, using perturbation expansions with respect to the assumed small amplitude of the breathing mode showed that, when the frequency of the radial motion of a single bubble happens to be twice the linear frequency of a shape mode, subharmonic excitation of the later mode occurs. Moreover, when the frequency of the radial motion happens to be equal to the linear frequency of a shape mode, harmonic resonance can arise. The former should arise first, as it is inversely proportional to the square of the excitation amplitude followed by the latter, as it

https://doi.org/10.1017/S0022112010006361 Published online by Cambridge University Press

is inversely proportional to the excitation amplitude, when this amplitude is much less than one. This is exactly what is observed in figure 8, although the amplitude here is large, $\varepsilon = 1$. The dominance of the P_2 mode throughout and more so towards the end of the simulations and its oscillation with a frequency similar to that of the breathing mode verifies that it is generated by the combined volume oscillation and linear translation of the bubbles and the squeezing that they apply to each other eventually, but not by some type of resonance. In other words, this mode is excited here by the same mechanism as was excited in the smaller bubbles.

The fact that in this case of interacting bubble pairs, shape deformations appear only at the rear side of both bubbles, although based on the Rayleigh–Taylor instability one would have anticipated the opposite, can be explained by extending the analysis of Batchelor (1987). He was intrigued by the fact that the upper surface of steadily rising gas bubbles, where the less dense gas displaces the more dense liquid, is stable, whereas the rear side often has ripples, and he showed that the pure straining motion of the liquid ahead of the bubble stretches the front bubble interface and convects whichever disturbance may arise there to the rear of the bubble. This is exactly the reason that as the bubbles approach each other and the parametric resonance excites the third Legendre mode, the front of the bubble always remains undisturbed by this mode.

Further increasing the bubble size to $R_b^* = 1\,\text{mm}$ gives rise to even higher surface modes, but the bubbles always deform at their rear side and flatten at their front side. On the contrary, decreasing the bubble radius below 5 μm increases the viscous effects so much that the oscillations are damped very fast even when the amplitude is increased. For example, when $R_b^* = 1\,\mu\text{m}$ and $D = 2.8$ with ε increased to either 1.5 or 2, the bubbles undergo up to 5 volume oscillations and their final distance is 2.56 and 2.45, respectively. Therefore, the bubble size of approximately $R_b^* = 5\,\mu\text{m}$ in water constitutes the lower limit below which the secondary Bjerknes force induced by a step change in pressure is ineffective to bring the bubbles close enough to lead to bubble merging. This, of course, does not necessarily imply that a continuously applied oscillatory forcing will not bring these bubbles together.

4.2.3. *Effect of initial bubble distance, D*

Retaining the size of the bubbles at $R_b^* = 30\,\mu\text{m}$ in water, we increase the initial distance between their centres from $D = 2.8$ to $D = 5$. Since the bubbles are now further apart, their interaction will be weaker and their average acceleration is expected to decrease. Hence, the time needed for the two bubbles to approach each other will be increased and larger shape deformations are allowed to arise, since there will be more time for the two bubbles to oscillate and accelerate. Figure 9 presents the time evolution of the acceleration of the centre of the left bubble for $D = 2.8$ and $D = 5$. Indeed, the average acceleration over the first period of volume oscillation is $\langle g \rangle = 1.231$ for $D = 2.8$, but decreases to $\langle g \rangle = 0.529$ for $D = 5$. However, as time proceeds and the bubbles approach each other, the amplitude of their periodic acceleration in each period of volume oscillation increases monotonically and eventually approaches the value of the initial acceleration of the bubbles at the smaller initial distance of $D = 2.8$. In this figure, we observe that, for both distances, the periods of the acceleration are in the range 0.308–0.328, which is close to the nonlinear period of the breathing mode (table 2). This indicates that bubble acceleration is generated by the volume oscillations, and it is not significantly affected by bubble deformation, at least when this is not too large. The translation of the centres of volume for $D = 2.8$ and $D = 5$ is given in figure 3 for easier comparison

https://doi.org/10.1017/S0022112010006361 Published online by Cambridge University Press

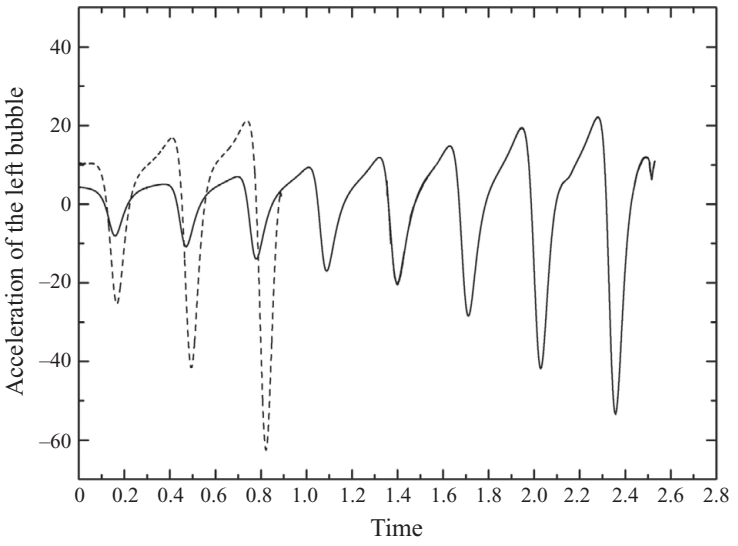

FIGURE 9. Time evolution of the acceleration of the left bubble for two different distances $D = 2.8$ (---) and $D = 5$ (—). The two bubbles are equal with $R_b^* = 30\,\mu\text{m}$, $Oh^{-1} = 46.701$, $P = 41.265$ and $\varepsilon = 1$.

with the other cases. As anticipated, the time needed for the two bubbles to approach each other increases with their distance. When the initial distance, D, is set at 2.8, simulations stop at $t = 0.914$, while when $D = 5$, simulations stop at $t = 2.61$, because of close proximity of the two bubbles. The evolution of the coefficients of the P_2–P_6 Legendre polynomials for $D = 5$ is given in Chatzidai (2008). Comparing them with the coefficients of the modes for $D = 2.8$ (figure 8) makes it plain that the final bubble shapes are less squeezed when they are initially closer together, although their initial acceleration is higher, and their deformations described by higher modes, such as P_3 and P_4, are less significant, since there was not enough time for them to increase.

Keeping the initial dimensionless distance at $D = 5$ and increasing the bubble size to $R_b^* = 100\,\mu\text{m}$, and even more to $R_b^* = 1\,\text{mm}$, results in even more deformed shapes. The deformations are limited again in the rear bubble side, while the front side remains almost spherical. Such shapes have also been reported by Pelekasis & Tsamopoulos (1993*a*, *b*), and have been called spherical-cap shapes, because of the resemblance of their front side to the classical spherical-cap shapes reported by Davis & Taylor (1950). Now computations stop before the two bubbles come very close together due to the large amplitude deformations. Figure 10 shows selected shapes of the two bubbles for the case with $R_b^* = 1\,\text{mm}$ in water ($Oh^{-1} = 269.63$, $P = 1375.51$, $\varepsilon = 1$, $D = 5$). The Fourier–Legendre decomposition of the bubble surface reveals that the lowest surface mode P_2 is again the dominant one throughout the simulation but after $t \cong 0.13$ even higher modes start to arise and finally the modes P_{12} and P_{13} dominate the shape of the bubble. This can be confirmed by noticing the 13 lumps in the bubble shapes in figure 10. Examination of the linear frequencies of the breathing mode and of the P_{12} and P_{13} modes at $\omega_o = 76.05$ (table 2), $\omega_{12} = 44.857$ and $\omega_{13} = 50.332$ verifies that these higher modes also arise through subharmonic resonance, i.e. a parametric instability. As should have been expected, in larger bubbles, capillarity is less effective and disturbances of shorter wavelength may arise, especially when these are excited by the parametric resonance. These disturbances should grow and lead to bubble breakup, which is known to occur, but not captured numerically as yet. Again,

https://doi.org/10.1017/S0022112010006361 Published online by Cambridge University Press

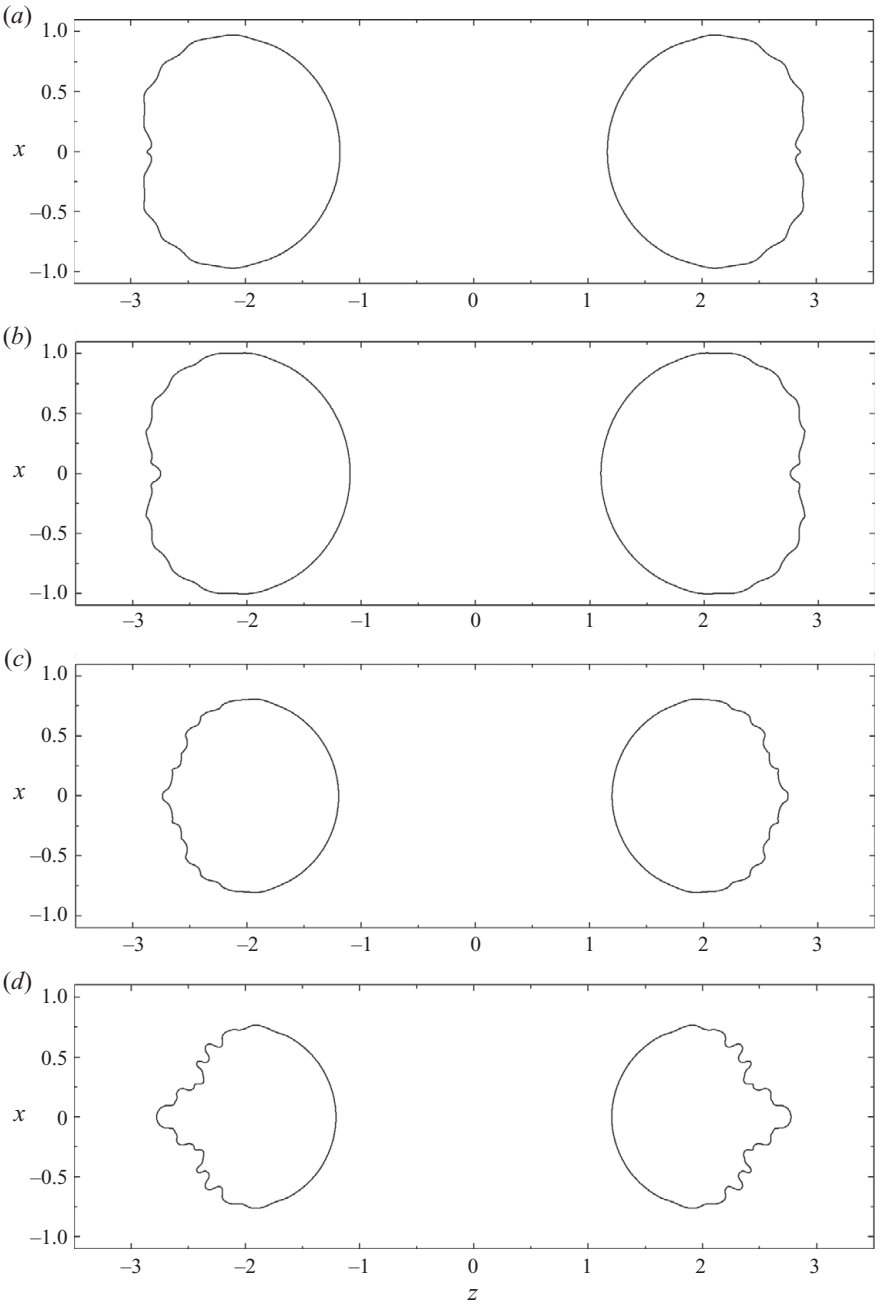

FIGURE 10. (*a–d*) Spherical cap shapes of the bubbles at $t = 0.15$, 0.165, 0.18 and 0.187, respectively, for two equal bubbles with $R_b^* = 1\,\text{mm}$, $Oh^{-1} = 269.63$, $P = 1375.51$, $\varepsilon = 1$ and $D = 5$.

isolated bubbles deformed in this way have been repeatedly observed experimentally (e.g. Kornfeld & Suvorov 1944; Ohl *et al.* 1999; Daglia & Poulain 2010; Versluis *et al.* 2010). These deformations have often led to the formation of multiple small satellite bubbles surrounding the parent bubble (Ohl *et al.* 1999). Formation of such satellite bubbles in only one side of a bubble, the one away from nearby walls, has also been

https://doi.org/10.1017/S0022112010006361 Published online by Cambridge University Press

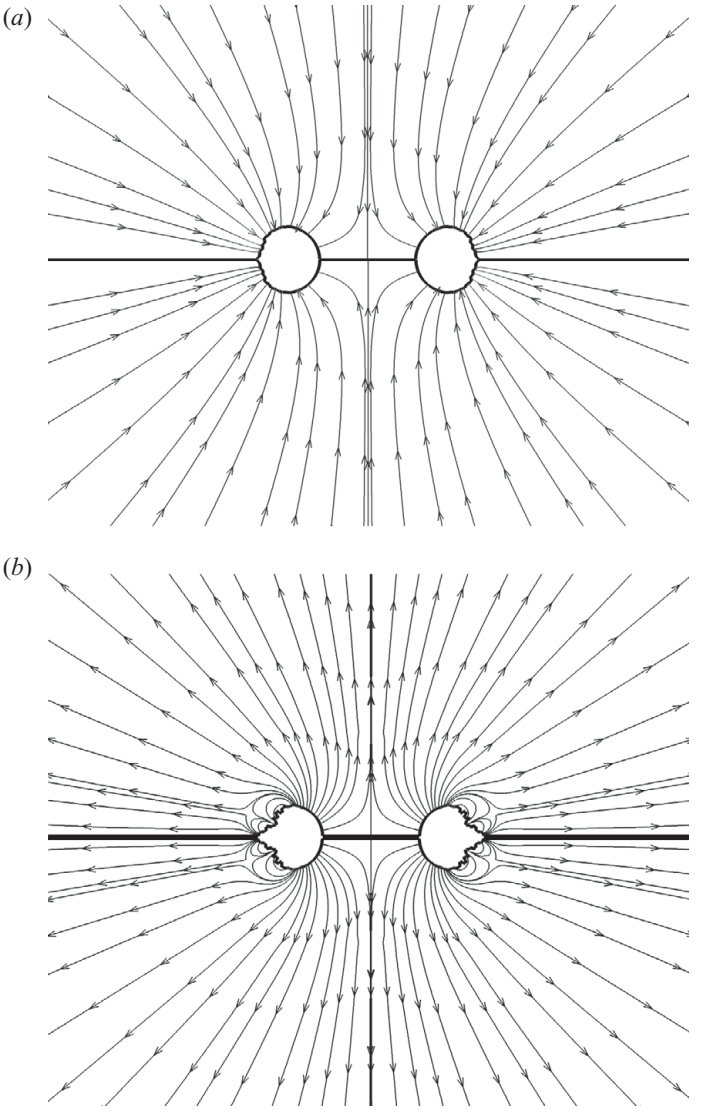

FIGURE 11. (a,b) Streamlines at $t = 0.179$ and 0.187 for two equal bubbles with $R_b^* = 1\,\mathrm{mm}$, $Oh^{-1} = 269.63$, $P = 1375.51$, $\varepsilon = 1$ and $D = 5$.

observed (Lauterborn 1972). Instantaneous streamlines for this case are given in figure 11. While the bubbles undergo contraction, the flow is towards them from infinity and away from them subsequently under expansion. Axisymmetric extensional flow takes place between them with oscillating direction contributing to the stabilization of this part of the bubble surface. The increased deformation on the bubble back side during expansion leads to closed streamlines there.

In an attempt to explain the formation of the so-called bubble grapes, it has been shown by Pelekasis *et al.* (2004) and Mettin *et al.* (1997) that bubbles at very large distances from each other in an oscillatory pressure field can accelerate towards or away from each other or remain at a constant distance after a very large number of cycles of volume oscillations. One of the basic assumptions made in these studies

https://doi.org/10.1017/S0022112010006361 Published online by Cambridge University Press

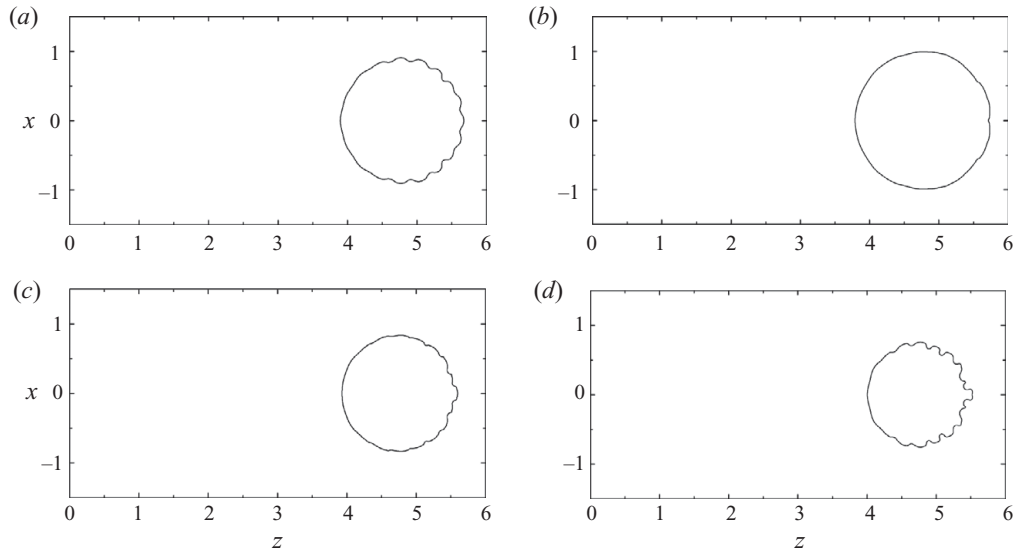

FIGURE 12. (*a–d*) Spherical-cap shapes of the right bubble at $t = 0.19,\ 0.2,\ 0.22$ and 0.226, respectively. The two bubbles are equal with $R_b^* = 1$ mm, $Oh^{-1} = 269.63$, $P = 1375.51$, $\varepsilon = 1$ and $D = 9.9$. The left bubble shapes are the mirror images of these.

was that the bubbles could retain their spherical shape and weak viscous effects were introduced, in the form of boundary layers around each bubble in the first of the above studies. To test the viability of large bubbles to retain their spherical shapes while they undergo volume oscillations and accelerate along their common axis, we examined bubbles of radius of 1 mm and increased their initial distance D to 9.9. This bubble size is larger whereas their distance is smaller than those examined in these papers. Hence, their interaction and acceleration will be stronger here, which should lead to shape instabilities faster. On the other hand, in the present model we have included viscous forces in full and examined a step change in pressure and not an oscillatory one, which could lead to resonance with the forcing frequency as well. This large interbubble distance requires more elements to be used in order to retain the accuracy of our computations, so mesh M5 is used. Unfortunately, this distance cannot be increased further, given our hardware/software configuration, without compromising accuracy. Fairly soon, the bubbles are seen to develop spherical-cap shapes and short waves on their back side, although one would have expected that capillarity and viscous damping could prevent the higher modes from growing. Owing to the corrugated surfaces and the microflow that arise within each trough we have refined the mesh, but the computations could not proceed much further even with the denser mesh.

Selected bubble shapes are given in figure 12 for the right bubble, while the left bubble will be symmetric, as the two bubbles are equal. Similar shapes for $R_b^* = 1$ mm, at a large initial distance between the two bubbles but for much lower disturbance amplitude, have been predicted by Pelekasis & Tsamopoulos (1993*a*) using a completely different code, based on boundary elements, and assuming irrotational flow. It is noteworthy that due to the absence of viscosity there, the bubble shape deformations were even sharper and these irregularities arose earlier (Pelekasis 1991). On the contrary, the shapes predicted here are much smoother because of the complete accounting of the effect of viscous forces. An examination of the Legendre coefficients

https://doi.org/10.1017/S0022112010006361 Published online by Cambridge University Press

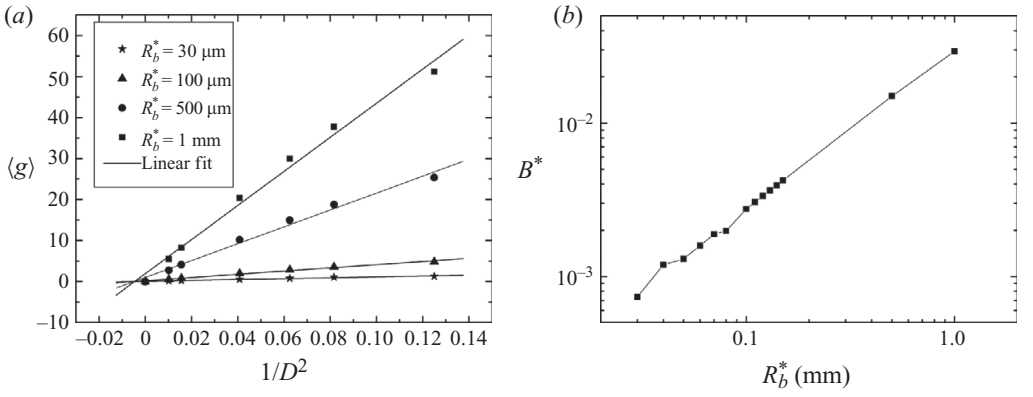

FIGURE 13. (*a*) Variation of the average acceleration of the left bubble with the initial distance between the two centres of volume for $R_b^* = 30\,\mu$m (⋆), $R_b^* = 100\,\mu$m (▲), $R_b^* = 500\,\mu$m (●) and $R_b^* = 1$ mm (■), and (*b*) variation of B^* with the bubble size for equal bubbles and $\varepsilon = 1$.

reveals that P_2 is the dominant mode until $t \cong 0.16$. Subsequently, modes higher than P_{15} start to increase abruptly and almost simultaneously (Chatzidai 2008). At $t \cong 0.2$, figure 12 shows that the bubbles tend to return to their spherical shape, as all higher modes become negligible and P_2 becomes the dominant mode again. A little later, the higher modes increase again. The period of the zeroth mode at the later stages of the simulation is found to be 0.058, while P_{19} oscillates with a period 0.0256 and modes P_{15}–P_{18} and P_{20} are oscillating with a period 0.032 approximately. This points to the possibility of a parametric instability through superharmonic resonance of all these modes with the breathing mode, although their eigenfrequencies are not exactly half the eigenfrequency of the breathing mode. According to Hall & Seminara (1980), this should follow the subharmonic and harmonic resonances, but their analysis assumed that ε is much smaller than 1, not equal to it, as it is here.

In order to examine whether the Bjerknes prediction that this force is inversely proportional to the square of the bubble distance still holds, we performed a number of computations with $R_b^* = 30,\ 100,\ 500$ and $1000\,\mu$m, when this distance is $D = 2.8,\ 3.5,\ 4,\ 5,\ 8$ and 9.9. The average acceleration is obtained as before over the first period of the particular volume oscillations. Figure 13(*a*) shows the resulting linear acceleration $\langle g \rangle$ values versus $1/D^2$ for all the above cases and the linear best fits to approximate the four data sets. The expressions for these lines along with the correlation coefficient, C, and the standard deviation, SD, are

$$\left.\begin{array}{llll} R_b^* = 30\,\mu\text{m}, & \langle g \rangle = 0.104 + 10.123/D^2, & C = 0.983, & SD = 0.092, \\ R_b^* = 100\,\mu\text{m}, & \langle g \rangle = 0.312 + 37.896/D^2, & C = 0.994, & SD = 0.203, \\ R_b^* = 500\,\mu\text{m}, & \langle g \rangle = 0.995 + 205.887/D^2, & C = 0.994, & SD = 1.067, \\ R_b^* = 1\,\text{mm}, & \langle g \rangle = 2.892 + 404.137/D^2, & C = 0.995, & SD = 0.2. \end{array}\right\} \quad (4.10a)$$

It can be safely concluded that the average acceleration, $\langle g \rangle$, scales linearly with $1/D^2$, even when the viscosity of water is accounted for. However, all linear fits are of the form

$$\langle g \rangle = A + B/D^2, \quad (4.10b)$$

with the size of the first coefficient on the right-hand-side much smaller than the second one. If only the larger bubble distances ($1/D^2 \leqslant 0.04$) are included in these linear fits, the magnitude of the intercepts decreases further, indicating that this

https://doi.org/10.1017/S0022112010006361 Published online by Cambridge University Press

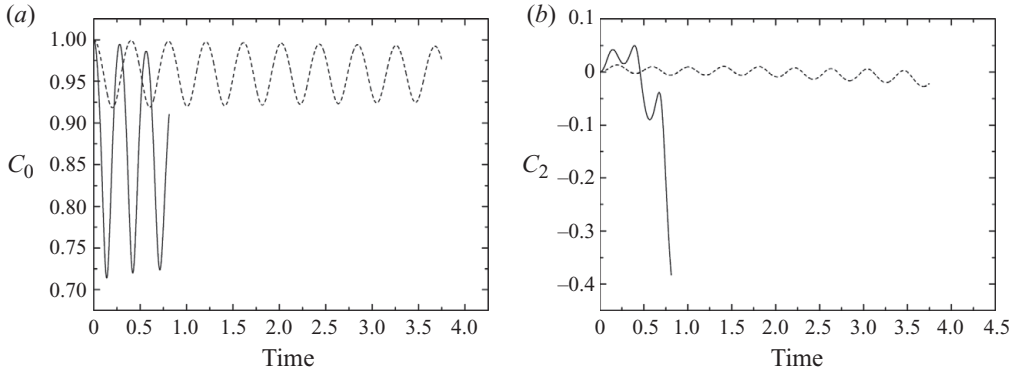

FIGURE 14. Time evolution of the coefficients of the Legendre polynomials (*a*) P_o and (*b*) P_2 for two different disturbance amplitudes, $\varepsilon = 0.2$ (---) and $\varepsilon = 1$ (—). The two bubbles are equal with $R_b^* = 40\,\mu\text{m}$, $Oh^{-1} = 53.926$, $P = 55.02$ and $D = 2.8$.

prediction does not contradict the asymptotic result (Bjerknes 1906; Doinikov 1999) that as the bubble distance approaches infinity, the attractive force will tend to zero.

Another important observation is related to the dependence of the Bjerknes force on bubble size. According to linear theory for inviscid liquids, it should depend on the product of the amplitude of volume pulsations of the two bubbles (Bjerknes 1906; Batchelor 1967; Pelekasis & Tsamopoulos 1993*a*, *b*). Plotting the slope B from (20*b*) in dimensional form versus the bubble radius in a linear–linear plot confirms that

$$B^* \sim R_b^*, \tag{4.11}$$

i.e. the Bjerknes force in viscous liquids is proportional to the bubble radius. This confirms that the asymptotic analysis by Doinikov (1999), which was derived for viscous liquids assuming spherical bubbles at very large distances from each other, holds even when all these assumptions are removed. The same dependence is given in figure 13(*b*) in a log–log scale to expand the range of smaller bubble sizes. In this way, a very small deviation from (4.11) is found for smaller bubbles, possibly because of the increased importance of viscous drag. In order to closely determine the size of bubbles below which this slope starts to deviate, we carried out simulations with additional bubble radii (Chatzidai 2008) and found only a very small decrease of the initial acceleration for bubbles of radius $R_b^* \leqslant 120\,\mu\text{m}$.

4.2.4. *Effect of the disturbance amplitude, ε*

Next, we examine the importance of the magnitude of the step change in pressure to initiate bubble attraction in a viscous liquid, since in typical experiments, amplitudes smaller than $\varepsilon = 1.2$–1.4 have been employed. As discussed in § 4.2.1, decreasing the disturbance amplitude increases the period of volume oscillations, because the pressure at infinity will increase less than before (see (4.4)). This should lead to a decrease in the average acceleration of the bubbles and consequently to an increase in the time needed for the two bubbles to approach each other. First, cases of bubbles up to 80 μm in water and initial distance $D = 2.8$ are examined. When $\varepsilon = 1$, it was shown that bubbles larger than 30 μm deform at their rear side. Decreasing the amplitude ε to 0.2, the bubbles remain almost spherical until the end of the simulations even when their initial radius is 80 μm. Figure 14 shows the coefficients C_0 and C_2 of the corresponding modes, for bubble radius 40 μm in water ($Oh^{-1} = 53.926$, $P = 55.02$), at an initial distance 2.8 with disturbance amplitudes 0.2 and 1. Clearly, the C_0 coefficient, which is

https://doi.org/10.1017/S0022112010006361 Published online by Cambridge University Press

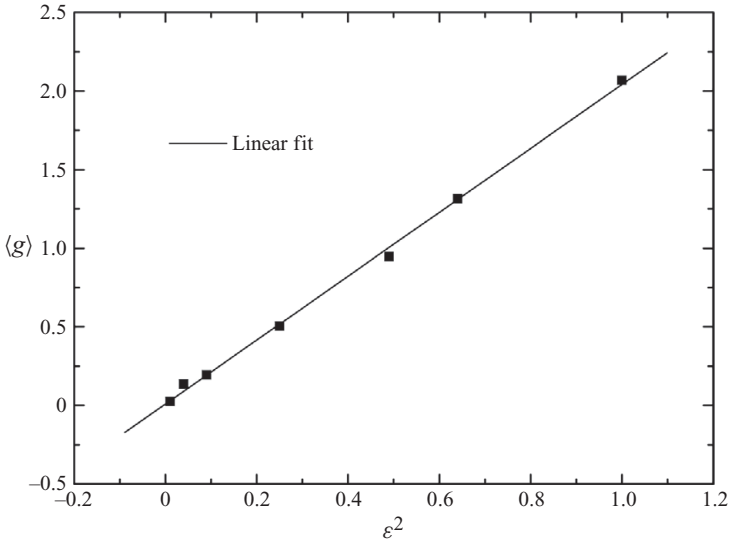

FIGURE 15. Variation of the average acceleration of the left bubble with the disturbance, ε, for $R_b^* = 40\,\mu\text{m}$, $Oh^{-1} = 53.926$, $P = 55.02$ and $D = 2.8$.

related to volume oscillations, demonstrates that when ε is decreased to 0.2, the period of volume oscillations increases, while their amplitude decreases, in comparison to the case with $\varepsilon = 1$. It is also noteworthy that for $\varepsilon = 0.2$, the value of the period (0.409) is very close to that predicted from linear theory $T_{o,\infty} = 0.407$; see table 2. When ε increases to 1, the period decreases to 0.285. Moreover, the smaller coefficient of the P_2 mode makes it clear that the bubble retains a more spherical shape until the end of the simulations when ε is decreased to 0.2, although it alternates between oblate and prolate configurations with a constant trend towards an oblate one. Figure 3 includes the evolution of the centres of volume of the two bubbles for these two cases as well. We find that the time needed for the two bubbles to approach each other increases, in the case of $\varepsilon = 0.2$, allowing the simulations to proceed to much longer times.

In order to examine whether the dependence of the acceleration on the disturbance still follows predictions for inviscid liquids (Batchelor 1967; Pelekasis & Tsamopoulos 1993*a*), i.e. it increases proportionately to ε^2, we also carried out simulations for $\varepsilon = 0.1$, 0.3, 0.5, 0.7 and 0.8. Figure 15 shows that indeed the average acceleration follows this dependence although the amplitudes used herein are as large as 1, while the linear expression that best fits these data points is

$$\langle g \rangle = 0.01 + 2.031\varepsilon^2. \tag{4.12}$$

This occurs as in Pelekasis & Tsamopoulos (1993*a*), in spite of the fact that the bubble radii are very small, and viscous effects are accounted in full here.

In order to directly compare with the results in figure 9 of Pelekasis & Tsamopoulos (1993*a*), we increased the bubble radius to 1 mm ($Oh^{-1} = 269.63$, $P = 1375.51$), set their initial distance at 2.5 and the amplitude to 0.3. In Pelekasis & Tsamopoulos (1993*a*), the average acceleration over the first period of volume oscillations was found to be 7.198, whereas it decreases here, as it should, to 6.72, because of viscous damping. Retaining all the physical parameters to their previous values, except for the initial interbubble distance, which we increase to 2.8, we find that the two bubbles deform at their rear side and flatten at the front, a picture similar to that of $\varepsilon = 1$. Because

https://doi.org/10.1017/S0022112010006361 Published online by Cambridge University Press

Case	$\langle g \rangle$	Re_{vi}/Re_{tr}	Ca_{vi}/Ca_{tr}	Bubble shape
1	0.248	113.236/1.304	0.311/0.004	Almost spherical
2	0.256	215.983/3.343	0.297/0.005	Almost spherical
3	0.724	421.072/9.571	0.289/0.007	Oblate
4	1.265	728.547/16.485	0.286/0.006	Spherical cap
5	0.543	728.547/6.406	0.286/0.003	Spherical cap
6	2.095	831.028/17.903	0.286/0.006	Spherical cap
7	0.137	831.028/0.216	$0.286/7.428 \times 10^{-5}$	Almost spherical
8	1.975	2060.709/56.36	0.283/0.008	Spherical cap
9	51.188	20505.25/675.691	0.282/0.009	Spherical cap
10	6.028	20505.25/73.69	0.282/0.001	Spherical cap
11	20.376	20505.25/227.432	0.282/0.003	Spherical cap
12	5.503	20505.25/60.747	$0.282/8.356 \times 10^{-4}$	Spherical cap
13	0.698	20505.25/7.792	$0.282/1.072 \times 10^{-4}$	Globally deformed

TABLE 4. The acceleration during the first period of oscillation, the vibration and translation Reynolds and capillary numbers and the observed final bubble shapes for the 13 cases in table 2.

of the lower disturbance in pressure at infinity, the time needed for the two bubbles to approach increases relative to when $\varepsilon = 1$, the average acceleration decreases and consequently the deformations of the bubble surfaces are less intense. If the initial distance between the two bubbles is increased further to 9.9 while the size of the bubbles remains at 1 mm and ε at 0.3, the average acceleration decreases, as seen in table 4. Now, the bubble shapes that arise towards the end of the simulations are wavy in both their front and rear sides. Such shapes were called 'globally deformed shapes' by Pelekasis & Tsamopoulos (1993*a*) and earlier observed by Kornefeld & Suvorov (1944) for isolated bubbles. These are clearly distinct from the 'spherical-cap' shapes predicted above when $\varepsilon = 1$ (figure 12). The smaller disturbance amplitude combined with the viscous resistance to flow produces a decrease in the average acceleration, and the streaming flow in the bubble front, which, in turn, is not sufficient to 'stabilize' the front bubble surface, as explained by Batchelor (1987).

Figure 16 shows the evolution of the shape of the right bubble for these parameters. As the time needed for the two bubbles to approach increases due to the large distance and the small disturbance, there is enough time for even higher and higher modes to arise. The Legendre decomposition (Chatzidai 2008) of the bubble shape shows that until $t \approx 0.45$, P_2 is the only mode that can be seen. After $t \approx 0.45$, higher modes start to appear and finally P_{10} and P_{11} become dominant in the bubble shape due to subharmonic resonance with the zeroth mode (Hall & Seminara 1980). Indeed, the eigenvalues are $c_0 = -0.0074 \pm 76.05\mathrm{i}$, $c_{10} = -1.013 \pm 34.55\mathrm{i}$ and $c_{11} = -1.204 \pm 39.59\mathrm{i}$, indicating that not only a very slow damping of the zeroth mode but also its eigenfrequency is twice as that of these two higher modes. The coupling of these shape modes here leads to the formation of a jet at the back side of the bubbles which is directed towards their front side (figure 16). The large shape deformation prevents obtaining converged solutions at later times, but it is reasonable to expect that this fast-moving jet will pierce the bubble before any other disturbance becomes appreciable and lead to a bubble of doughnut shape. The formation of a jet on the side of a cavitation bubble away from a nearby solid wall and moving towards this wall has been predicted theoretically (Plesset & Chapman 1971; Blake, Taib & Doherty 1986; Popinet & Zaleski 2002) and observed experimentally (Lauterborn & Bolle 1975; Tomita & Shima 1986; Vogel, Lauterborn & Timm 1989). In the present

https://doi.org/10.1017/S0022112010006361 Published online by Cambridge University Press

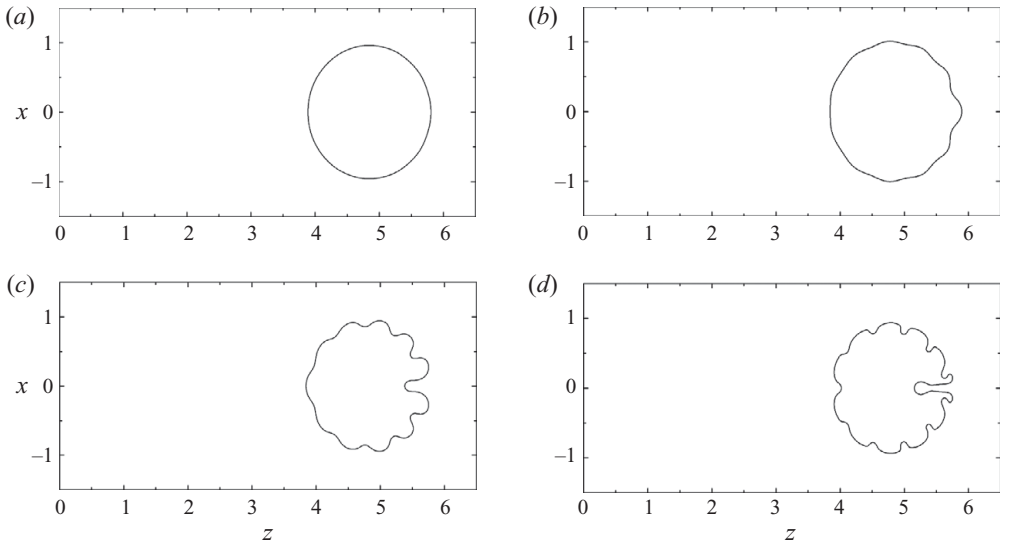

FIGURE 16. (*a–d*) Shapes of the right bubble at $t = 0.5,\ 0.55,\ 0.6$ and 0.651, respectively. The two bubbles are equal with $R_b^* = 1$ mm, $Oh^{-1} = 296.63$, $P = 1375.51$, $\varepsilon = 0.3$ and $D = 9.9$. At the later stages of the simulation, globally deformed shapes arise.

case of interacting bubbles of equal size, the symmetry plane between the bubbles introduces the same boundary conditions as a solid wall would have on a single bubble. Therefore, it is not surprising that we predict here the formation of a jet at this particular location on the bubble surface and directed towards the other bubble.

Pelekasis & Tsamopoulos (1993*a*) determined that the appearance of the two distinct types of bubble shapes observed in their inviscid simulations, namely 'spherical cap shapes' and 'globally deformed shapes', depended on the Bond number, $Bo = (\langle g^* \rangle\ R_b^* \rho^* / \sigma^*)$, which measures the relative importance of acceleration and surface tension. When the ambient pressure was 1 atmosphere, they found that when $Bo > 1.5$, spherical-cap shapes appear, whereas when $Bo < 1$ the entire interface deformed. For a pair of equal bubbles and following the present characteristic scales, Bo is identical to the dimensionless average acceleration $\langle g \rangle$. Thus, we can readily examine whether a similar rule applies when viscous forces are included in the model. Table 4 presents several of the cases which we have computed until either the bubbles came too close to each other or formed large bubble distortions, and the final shapes observed in each case. We predict globally deformed shapes only in one simulation with large bubbles of 1 mm, resulting in a large Oh^{-1}, i.e. negligible viscous effects, when they are far apart and under a small pressure perturbation. In the table, we also present the Reynolds and capillary numbers based either on bubble initial translation or vibration velocity, defined as

$$Re_{tr} = \frac{\rho^* \overline{U} U_{ch}^* R_b^*}{\mu^*}, \quad Re_{vi} = \frac{\rho^* R_b^{*2} \omega_o^*}{\mu^*}, \quad Ca_{tr} = \frac{\mu^* \bar{U} U_{ch}^*}{\sigma^*}, \quad Ca_{vi} = \frac{\mu^* R_b^* \omega_o^*}{\sigma^*}. \quad (4.13)$$

It is observed that globally deformed shapes were obtained only in case 13, where Re_{vi} assumes its largest value favouring surface instabilities and Re_{tr} is quite small, preventing convective smoothing of the bubble front surface. Clearly, all these factors allow high surface modes to appear and remain after extended oscillation and interaction between the bubbles. On the contrary, as the bubble size decreases, Oh^{-1} and P decrease, leading to higher viscous and capillary forces, and as the disturbance

https://doi.org/10.1017/S0022112010006361 Published online by Cambridge University Press

amplitude increases, the bubble interaction time decreases. All these favour the formation of bubbles that are either slightly deformed or have spherical cap shapes. Of the simulation results presented in table 4, only six reached accelerations less than one and in only two of them the interbubble distance was more than 2.8, to allow enough time for the bubbles to interact and translate. First of these two is case 13 and the second is case 5, which is the only case that does not follow the rule observed by Pelekasis & Tsamopoulos (1993*a*). In other words, fluid viscosity enhances the stabilizing effect of the extensional flow at the front side of the bubble. Table 4 also demonstrates that both Re_{vi} and Re_{tr} increase with the bubble radius and the latter is more than an order of magnitude smaller than the former, validating the assumptions of Pelekasis *et al.* (2004).

4.3. *Other damping mechanisms*

4.3.1. *Liquid compressibility*

Often, in bubble collapse studies, its surface velocity may reach an appreciable fraction of the velocity of sound in the liquid, raising the question as to how liquid compressibility could affect the bubble dynamics studied herein. Moreover, it is known that liquid compressibility slowly damps oscillations of isolated bubbles (see Keller & Miksis 1980). When liquid compressibility is accounted for, (2.2)–(2.4) are modified as follows:

$$\frac{\rho_c^*}{\rho^*}\frac{\mathrm{D}\boldsymbol{u}}{\mathrm{D}t} - \nabla\cdot\boldsymbol{\sigma} = 0, \tag{4.14}$$

$$\frac{\partial}{\partial t}\left(\frac{\rho_c^*}{\rho^*}\right) + \nabla\cdot\left(\frac{\rho_c^*}{\rho^*}\boldsymbol{u}\right) = 0, \tag{4.15}$$

$$\boldsymbol{\sigma} = -P\boldsymbol{I} + \frac{\mu_c^*}{\mu^*}Oh\left[(\nabla\boldsymbol{u} + (\nabla\boldsymbol{u})^{\mathrm{T}}) - \frac{2}{3}(\nabla\cdot\boldsymbol{u})\boldsymbol{I}\right], \tag{4.16}$$

where ρ_c^* and μ_c^* are the density and viscosity of the liquid accounting for its compressibility, respectively. The former is determined by the modified Tait equation (Prosperetti & Lezzi 1986; Fujikawa & Akamatsu 1980):

$$\left(\frac{\rho_c^*}{\rho^*}\right)^n = \frac{P_c^* + B^*}{P_\infty^* + B^*}, \tag{4.17}$$

where P_∞^* is the far-field pressure and using $B^* = 3049.13$ bar and $n = 7.15$, (4.17) describes quite accurately the behaviour of water. The latter property also depends on the liquid pressure (Yasui 1995):

$$\mu_c^* = A^*\exp(B_1^* P_c^*), \tag{4.18}$$

where the dimensional constants are given by $A^* = 1.0019 \times 10^{-3}$ Pa s and $B_1^* = 7 \times 10^{-10}$ Pa^{-1} for water at 20°C.

In order to compare with our previous results, we repeat the simulations of § 4.2.1 for the bubble radius of 5 μm, but including liquid compressibility. Now, doubling the far-field pressure to 13.756 generates a spherical wave, which is transmitted inwards, towards the bubbles, with a finite speed. Before reaching the bubbles, the maximum pressure increases locally up to ∼18. When the wave reaches the back side of each bubble, it deforms the bubble only slightly, but more importantly it pushes it towards the other bubble. As the pressure wave continues to interact with the bubbles proceeding towards the centre, it is partially reflected on their surfaces and forms an expansion wave. Subsequently, the bubbles start to expand. Coupling the reflection of the pressure wave with the bubble expansion leads to a pressure wave

https://doi.org/10.1017/S0022112010006361 Published online by Cambridge University Press

with a more complicated shape and much larger pressure locally (as high as 100 at $t \sim 0.2$). Such maxima have also been also reported by Johnsen & Colonius (2009). In spite of this strong and uneven pressure field, the strong capillary force in these small bubbles allows them to keep their spherical shape. However, these high-pressure waves lead to volume oscillations with higher amplitude and consequently higher acceleration of the two bubbles. Similarly, Toilliez & Szeri (2008) have predicted an increased acceleration of bubble translation due to the primary Bjerkens force when liquid compressibility is accounted for. Moreover, comparing the evolution of the volume of the left bubble in figure 17(*a*), we observe that although the period of volume oscillation is nearly the same, the amplitude is higher when compressibility is accounted for. For a finite time at the beginning of the simulations, the volume of the bubble remains constant, indicating the time delay for the pressure wave to reach the bubble wall. Thereafter, the volume starts to decrease with an increasing bubble wall velocity, contributing to the pressure rise in the liquid near the bubble. The strongly varying pressure around the bubbles makes the oscillation of its volume slightly more complex when the second period starts.

Thereafter, the pressure slowly becomes more uniform throughout the liquid. Another consequence of the large pressure maxima periodically reaching the bubbles is that it takes them about half the time to approach each other compared to that in an incompressible liquid, as seen in figure 17(*b*). Their larger acceleration towards each other produces more flattened shapes at their fronts, as seen in figure 17(*c*). Finally, compressibility seems to have increased the damping of the bubble oscillations only slightly. Although we have examined a bubble of radius only 5 μm, i.e. in the low end of bubble sizes examined, yielding higher radial velocities, the predicted highest velocity during this simulation is only 1.304 $\mathrm{m\,s^{-1}}$. Given that the speed of sound in water at 20°C is 1481 $\mathrm{m\,s^{-1}}$, the resulting Mach number is only 0.0009, making it plain that liquid compressibility should not affect the bubble interactions studied herein.

4.3.2. *Thermal damping*

Depending on the bubble size and its natural or forcing frequency, if one is applied, heat conduction inside the bubble could induce damping in its oscillation. Moreover, its natural frequency depends on the thermal behaviour of the gas, which can range from adiabatic to isothermal. In general, if the driving frequency is relatively low, or the bubble radius is relatively small, then the time required for heat to flow in or out of the bubble is short with respect to an acoustic period. The temperature of the gas remains effectively constant across the bubble diameter and the bubble is said to behave isothermally. On the other hand, if the driving frequency is relatively high, or the bubble is relatively large, then the time required for heat to flow in and out of the bubble is long with respect to an acoustic period. In this case, there are significant temperature gradients across the bubble diameter and the system is said to behave adiabatically.

For the free oscillations examined here, we will employ the results of the linear theory developed by Chapman & Plesset (1971) to estimate the additional damping caused by heat conduction in the bubble, expressed by the additional coefficient of the thermal viscosity, $\mu_{th} = \mu^*_{th}/\mu^*$, and also the affected polytropic exponent, κ. These are obtained after numerically solving (17), (24)–(25) and (31) as given in Chapman and Plesset (1971). The thermophysical properties of air used are $\rho^*_g = 1.29\,\mathrm{kg\,m^{-3}}$, $k^* = 0.0247\,\mathrm{W\,(m\,K)^{-1}}$ and $C^*_v = 714.29\,\mathrm{kJ\,(kg\,K)^{-1}}$. To isolate the effect of thermal damping, the surrounding liquid is considered incompressible. The momentum and mass conservation (2.2) and (2.3) remain the same, while the total stress tensor is

https://doi.org/10.1017/S0022112010006361 Published online by Cambridge University Press

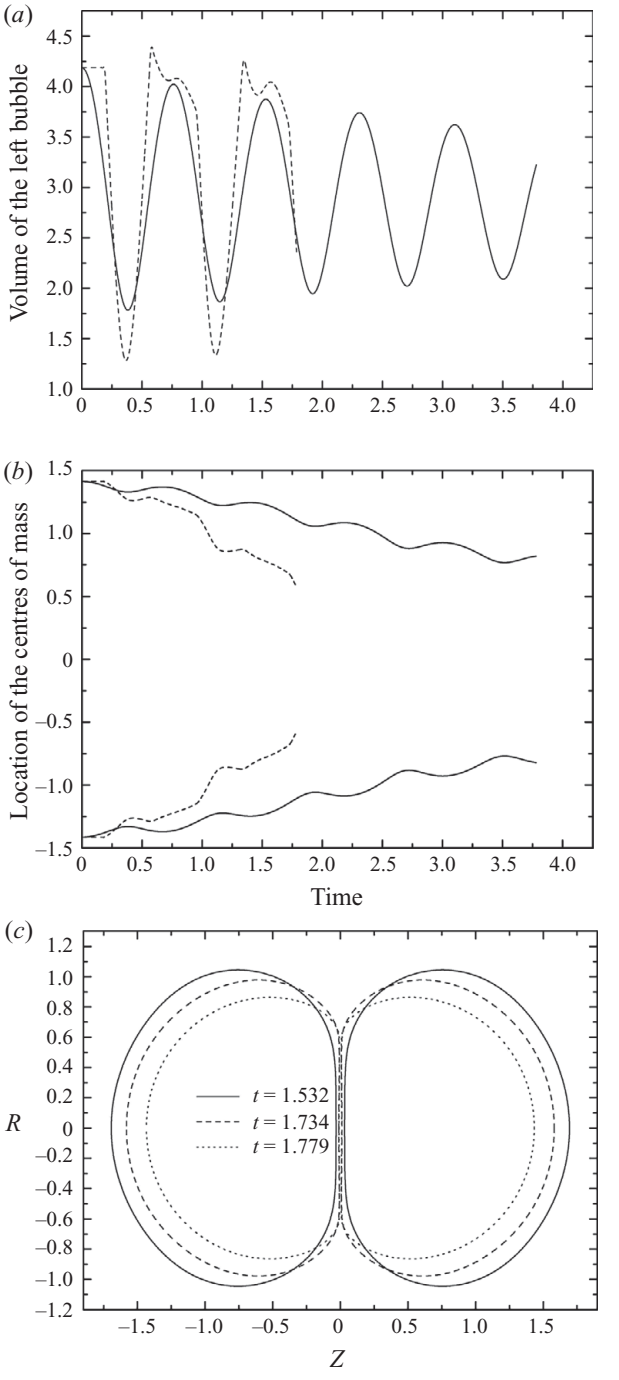

FIGURE 17. Time evolution of (*a*) the volume of the left bubble and (*b*) the centres of volume of the two bubbles both for an incompressible (—) and a compressible (---) liquid and (*c*) bubble shapes towards the end of simulations. The two bubbles are equal, with the same parameters as in figure 2, except that liquid compressibility is accounted for.

https://doi.org/10.1017/S0022112010006361 Published online by Cambridge University Press

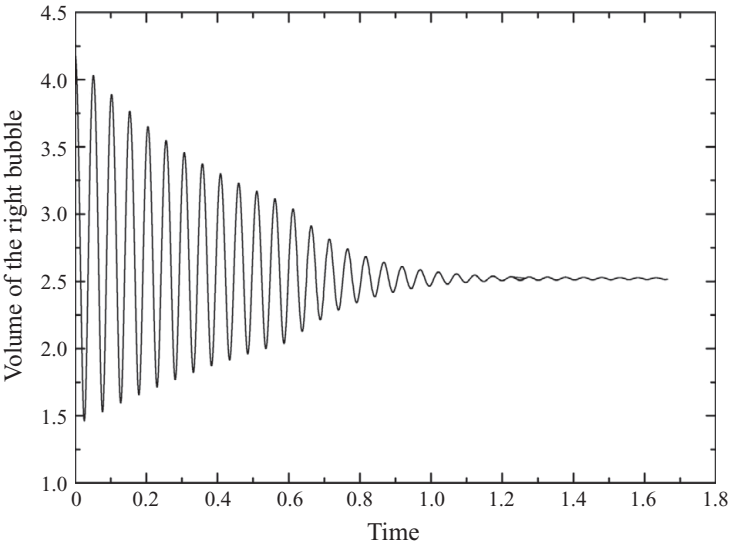

FIGURE 18. Time evolution of the volume of the right bubble. The two bubbles are equal with $R_b^* = 1$ mm, $Oh^{-1} = 269.63$, $P = 1375.51$, $\varepsilon = 1$ and $D = 9.9$.

given by

$$\boldsymbol{\sigma} = -P\boldsymbol{I} + Oh(1 + \mu_{th})[(\nabla \boldsymbol{u} + (\nabla \boldsymbol{u})^{\mathrm{T}})]. \tag{4.19}$$

As the effective viscosity of the liquid will now increase, it is expected that the amplitude of volume oscillations will decrease and, hence, the mutual Bjerknes forces will decrease and last for shorter times. We considered both small (5 μm) and large (1 mm) bubbles and set the initial distance of the two bubbles at $D = 9.9$ and the disturbance amplitude at $\varepsilon = 1$. As expected from the results of Chapman & Plesset (1971) for the smaller bubbles, thermal damping is of the order of the viscous damping, $\mu_{th} \approx 3$, and the gas behaves isothermally, $\kappa = 1.03$. This was confirmed by the results of our complete dynamic simulations, which also demonstrated little deviation from the previous ones.

On the contrary, more interesting is the case of large bubbles, for which we obtain $\mu_{th} = 124$ and $\kappa = 1.36$, i.e. the gas behaves adiabatically. In this case, large-amplitude deformations appeared at the bubble surface when they were at moderate or large distance from each other (figures 10 and 12). As can be seen in figure 18, although the period is not affected, the amplitude of the volume oscillation quickly decreases down to zero. This occurs after about 20 periods of oscillation. Until then, the two bubbles approach each other, but at the end their distance decreases by only 10 %. The much larger effective viscosity helps the bubbles to maintain their nearly spherical shape. Similar is the picture for initial distance between the two bubbles of $D = 5$. Of course, an accurate evaluation of the thermal behaviour and the motion and deformation of the bubbles requires the simultaneous solution of the mass, momentum and energy equations for the liquid and the bubble, combined with appropriate boundary conditions at the bubble surface. Such simulations are beyond the goals of this study.

5. Concluding remarks

The motion of two gas bubbles immersed in pure water and subjected to a step change in ambient pressure at the far field was studied. The present study covered

https://doi.org/10.1017/S0022112010006361 Published online by Cambridge University Press

a wide range of bubble sizes, 1 μm–1 mm. In contrast to previous works, viscous forces were fully accounted for and shape deformations were allowed. In fact, this is the first direct numerical simulation of this problem. Our newly developed finite element methodology, based on generating the computational mesh, to follow the large deformations of the bubbles and to become finer near the bubble surfaces in order to resolve the sharp boundary layers that develop there as the bubble sizes increase, proved to be accurate, robust and versatile. The step change in pressure induces volume oscillations on the two bubbles. The volume oscillations of one bubble generate a secondary pressure field to the ambient liquid which accelerates the other bubble along their common axis of symmetry. This acceleration is known as 'secondary Bjerknes effect' and, according to linear theory, when viscosity and bubble deformations are neglected it has been shown to be proportional to the amplitude of volume pulsations of the two bubbles and inversely proportional to the distance squared of their centres.

In the present study, we have demonstrated that the principle of the 'secondary Bjerknes law' applies for viscous fluids and deformable bubbles as well, but there are certain new aspects to it. (i) The constant of proportionality in this law depends on the viscous drag only for bubble radii in the lower end of the range we examined and more so when liquids more viscous than water are involved. (ii) Even when viscous effects are fully accounted for, bubble deformation seems to be the rule rather than the exception for bubbles with $R_b^* \geqslant 100\,\mu\text{m}$ and seems to lead to their breakup in spite of the stabilizing effects of capillary and viscous forces. It seems that when additional damping caused by heat transfer in the bubble is accounted for, shape deformations are prevented, especially for larger bubbles. (iii) Their interaction force increases and, hence, the time needed for the two bubbles to approach each other decreases with increasing Oh^{-1} and dimensionless pressure P and the increase applied to it to set them in motion, all three of these parameters decrease the period of the breathing mode. (iv) Even a large step increase in the ambient pressure is ineffective for bubbles in pure water with $R_b^* < 5\,\mu\text{m}$ and for more viscous than water liquids even for larger bubbles. (v) A step change in pressure always leads to bubble attraction, although the amplitude of the disturbance was very large, in agreement with the linear analysis, possibly because the viscous damping decreased the oscillation amplitudes and the duration of the interaction, both of which are necessary to observe deviations from this analysis (Pelekasis *et al.* 2004). (vi) Our predictions are in agreement with those of Doinikov (1999), although we have allowed the bubbles to be very close to each other and to deform. (v) Liquid compressibility does not seem to have an appreciable effect on bubble interaction.

More specifically, as the size of the bubbles increases and consequently Oh^{-1} increases, surface modes arise through parametric resonance of order which depends on their eigenvalues, which, in turn, depend on their size and applied disturbance in pressure. Increasing the interbubble distance affects bubble deformation by giving them more time to develop. When their initial distance is quite small, the bubbles remain almost spherical until the end of the computations when their size is very small ($< 5\,\mu\text{m}$), or they take an oblate shape for $5\,\mu\text{m} < R_b^* \leqslant 20\,\mu\text{m}$, or finally deformations arise and are kept at their rear side for $R_b^* > 20\,\mu\text{m}$, because of the stabilizing influence of the pure straining motion at the front of the bubbles. Increasing their initial distance D for relatively large bubbles $R_b^* \geqslant 100\,\mu\text{m}$, instabilities increase substantially. When the two bubbles are set far enough from each other, globally deformed shapes appear. Decreasing the disturbance amplitude, ε, the time needed for the deformations to appear increases, while the

https://doi.org/10.1017/S0022112010006361 Published online by Cambridge University Press

bubbles remain almost spherical till the end of the computations even for $R_b^* = 80\,\mu\text{m}$.

This work was partially supported by the PENED 2001 programme of the General Secretariat of Research and Technology of Greece (programme number PENED 2001-01ED558). Certain comments by the referees helped us improve the presentation of this work. We are thankful to Dr Pascal Hènon from INRIA for providing his library and his assistance on parallelization issues and to Professor Lauterborn for many helpful discussions.

REFERENCES

Batchelor, G. K. 1967 *An Introduction to Fluid Dynamics*. Cambridge University Press.

Batchelor, G. K. 1987 The stability of a large gas bubble rising through liquid. *J. Fluid Mech.* **184**, 399–422.

Bjerknes, V. F. K. 1906 *Fields of Force*. Columbia University Press.

Bjerknes, V. F. K. 1909 *Die Craftfelder*. Vieweg.

Blake, J. R., Taib, B. B. & Doherty, G. 1986 Transient cavities near boundaries. Part 1. Rigid boundary. *J. Fluid Mech.* **170**, 479–497.

Brennen, C. E. 1995 *Cavitation and Bubble Dynamics*. Oxford University Press.

Brenner, M. P., Hilgenfeldt, S. & Lohse, D. 2002 Single-bubble sonoluminescence. *Rev. Mod. Phys.* **74**, 425–484.

Chapman, R. B. & Plesset M. S. 1971 Thermal effects in the free oscillation of gas bubble. *J. Basic Engng* **93**, 373–376.

Chatzidai, N., Giannousakis, A., Dimakopoulos, Y. & Tsamopoulos, J. 2009 On the elliptic mesh generation in domains containing multiple inclusions and undergoing large deformations. *J. Comput. Phys.* **228**, 1980–2011.

Chatzidai, N. K. 2008 Motion, deformation and interaction of bubbles due to gravity and/or variation of the pressure of the ambient fluid. PhD thesis, University of Patras.

Chen, L., Li, Y. & Manasseh, R. 1998 The coalescence of bubbles: a numerical study. In *Third International Conference on Multiphase Flow*, ICMF'98, Lyon, France.

Crum, L. A. 1975 Bjerknes forces on bubbles in a stationary sound field. *J. Acoust. Soc. Am.* **57**, 1363–1370.

Daglia, R. & Poulain, C. 2010 When sound slows down bubbles. *Phys. Fluids* **22**, 041703.

Davies, R. M. & Taylor, G. I. 1950 The mechanics of large bubbles rising through extended liquids and through liquids in tubes. *Proc. R. Soc. Lond.* A **200**, 275–390.

Dimakopoulos, Y. & Tsamopoulos, J. 2003*a* A quasi-elliptic transformation for moving boundary problems with large anisotropic deformations. *J. Comput. Phys.* **192**, 494–522.

Dimakopoulos, Y. & Tsamopoulos, J. A. 2003*b* Transient displacement of a Newtonian fluid by air in straight and suddenly constricted tubes. *Phys. Fluids* **15** (7), 1973–1991.

Doinikov, A. A. 1999 Bjerknes forces between two bubbles in a viscous fluid. *J. Acoust. Soc. Am.* **106**, 3305–3312.

Doinikov, A. A. & Zavtrak, S. T. 1995 On the mutual interaction of two gas bubbles in a sound field. *Phys. Fluids* **7** (8), 1923–1930.

Feng, Z. & Leal, G. 1997 Nonlinear bubble dynamics. *Annu. Rev. Fluid Mech.* **29**, 201–243.

Foteinopoulou, K., Mavrantzas, V., Dimakopoulos, Y. & Tsamopoulos, J. A. 2006 Numerical simulation of multiple bubbles growing in a Newtonian liquid filament undergoing stretching. *Phys. Fluids* **18** (4), 042106 (1–24).

Fujikawa, S. & Akamatsu, T. 1980 Effects of the non-equilibrium condensation of vapour on the pressure wave produced by the collapse of a bubble in a liquid. *J. Fluid Mech.* **97**, 481–512.

Gaidamour, J. & Hènon, P. 2008 A parallel direct/iterative solver based on a Schur complement approach. In *11th IEEE Intl Conf. Computational Science and Engineering*, Sao Paulo, Brazil, pp. 98–105.

Goldberg, B. B., Raichlen, J. S. & Forsberg, F. 2001 *Ultrasound Contrast Agents: Basic Principles and Clinical Applications*. Dunitz Martin.

https://doi.org/10.1017/S0022112010006361 Published online by Cambridge University Press

Hall, P. & Seminara, G. 1980 Nonlinear oscillations of non-spherical cavitation bubbles in acoustic fields. *J. Fluid Mech.* **101**, 423–444.

Hènon, P. & Saad, Y. 2006 A parallel multistage ILU factorization based on a hierarchical graph decomposition. *SIAM J. Sci. Comput.* **28** (6), 2266–2293.

Johnsen, E. & Colonius, T. 2009 Numerical simulations for non-spherical bubble collapse. *J. Fluid Mech.* **629**, 231–262.

Karapetsas, G. & Tsamopoulos, J. 2006 Transient squeeze flow of viscoplastic materials. *J. Non-Newtonian Fluid Mech.* **133**, 35–56.

Keller, J. B. & Miksis, M. 1980 Bubble oscillations of large amplitude. *J. Acoust. Soc. Am.* **68**, 628–633.

Kornfeld, M. & Suvorov, L. 1944 On the destructive action of cavitation. *J. Appl. Phys.* **15**, 495–506.

Lauterborn, W. 1972 High-speed photography of laser-induced cavities in liquids. In *10th Intl Congress on High Speed Cinematography*, Nice, pp. 306–309.

Lauterborn, W. & Bolle, H. 1975 Experimental investigations of cavitation-bubble collapse in the neighbourhood of a solid boundary. *J. Fluid Mech.* **72**, 391–399.

Lauterborn, W., Kurz, T., Geisler, R., Schanz, D. & Lindau, O. 2007 Acoustic cavitation, bubble dynamics and sonoluminescence. *Ultrason. Sonochem.* **14**, 484–491.

Lauterborn, W., Kurz, T., Mettin, R. & Ohl, C. 1999 Experimental and theoretical bubble dynamics. In *Advances in Chemical Physics* (ed. I. Prigogine & S. A. Rice) vol. 110, Ch. 5, pp. 295–380. Wiley

Lehoucq, R. B., Sorensen, D. C. & Young, C. 1998 *ARPACK User's Guide: Solution of Large-Scale Eigenvalue Problems with Implicitly Restarted Arnoldi Methods.* SIAM.

Leighton, T. G. 1994 *The Acoustic Bubble*. Academic Press.

Li, T., Tachibana, K., Kuroki, M. & Kuroki, M. 2003 Gene transfer with echo-enhanced contrast agents: comparison between Albunex, Optison and Levovist in mice: initial results. *Radiology* **229**, 423–428.

Mettin, R., Akhatov, I., Parlitz, U., Ohl, C. D. & Lauterborn, W. 1997 Bjerknes forces between small cavitation bubbles in a strong acoustic field. *Phys. Rev.* E **56**, 2924–2931.

Miller, C. A. & Scriven, L. E. 1968 The oscillations of a fluid droplet immersed in another fluid. *J. Fluid Mech.* **32**, 417–435.

Nayfeh, A. H. & Mook, D. T. 1979 *Nonlinear Oscillations.* John Willey.

Oguz, H. & Prosperetti, A. 1990 A generalization of the impulse and virial theorems with an application to bubble oscillations. *J. Fluid Mech.* **218**, 143–162.

Ohl, C., Kurz, T., Geisler, R., Lindau, O. & Lauterborn, W. 1999 Bubble dynamics, shock waves and sonoluminescence. *Proc. R. Soc. Lond.* A **357**, 269–294.

Papanastasiou, T. C., Malamataris, N. & Elwood, K. 1992 A new outflow boundary condition. *Intl J. Numer. Meth. Fluids* **14**, 587–608.

Pelekasis, N. A. 1991 A study on drop and bubble dynamics via a hybrid boundary element-finite element methodology. PhD thesis, State University of New York at Buffalo.

Pelekasis, N. A., Gaki, A., Doinikov, A. & Tsamopoulos, J. A. 2004 Secondary Bjerknes forces between two bubbles and the phenomenon of acoustic streamers. *J. Fluid Mech.* **500**, 313–347.

Pelekasis, N. A. & Tsamopoulos, J. A. 1993*a* Bjerknes forces between two bubbles. Part 1. Response to a step change in pressure. *J. Fluid Mech.* **254**, 467–499.

Pelekasis, N. A. & Tsamopoulos, J. A. 1993*b* Bjerknes forces between two bubbles. Part 2. Response to an oscillatory pressure field. *J. Fluid Mech.* **254**, 501–527.

Plesset, M. 1954 On the stability of fluid flows with spherical symmetry. *J. Appl. Phys.* **25**, 96–98.

Plesset, M. S. & Chapman, R. B. 1971 Collapse of an initially spherical vapour cavity in the neighbourhood of a solid boundary. *J. Fluid Mech.* **47** (2), 283–290.

Plesset, M. S. & Prosperetti, A. 1977 Bubble dynamics and cavitation. *Annu. Rev. Fluid Mech.* **9**, 145–185.

Popinet, St. & Zaleski, St. 2002 Bubble collapse near a solid boundary: a numerical study of the influence of viscosity. *J. Fluid Mech.* **464**, 137–163.

Prosperetti, A. & Lezzi, A. 1986 Bubble dynamics in a compressible liquid. Part 1. First-order theory. *J. Fluid Mech.* **168**, 457–478.

https://doi.org/10.1017/S0022112010006361 Published online by Cambridge University Press

Rayleigh, Lord 1917 On the pressure developed in a liquid during the collapse of a spherical cavity. *Phil. Mag.* **34**, 94–98.

Toilliez, J. O. & Szeri, A. J. 2008 Optimized translation of microbubbles driven by acoustic fields. *J. Acoust. Soc. Am.* **123**, 1916–1930.

Tomita, Y. & Shima, A. 1986 Mechanisms of impulse pressure generation and damage pit formation by bubble collapse. *J. Fluid Mech.* **169**, 535–564.

Tsamopoulos, J. & Brown, R. A. 1983 Non-linear oscillations of inviscid drops and bubbles. *J. Fluid Mech.* **127**, 519–537.

Tsamopoulos, J., Dimakopoulos, Y., Chatzidai, N., Karapetsas, G. & Pavlidis, M. 2008 Steady bubble rise and deformation in Newtonian and Viscoplastic fluids and conditions for their entrapment. *J. Fluid Mech.* **601**, 123–164.

Tsiglifis, K. & Pelekasis, N. 2007 Nonlinear oscillations and collapse of elongated bubbles subject to weak viscous effects: effect of internal overpressure. *Phys. Fluids* **19**, 072106 (1–15).

Tsiglifis, K. & Pelekasis, N. 2008 Nonlinear radial oscillations of encapsulated microbubbles subject to ultrasound: the effect of membrane constitutive law. *J. Acoust. Soc. Am.* **123** (6), 4059–4070.

Versluis, M., Goertz, D., Palanchon P., Heitman I., van der Meer, S., Dollet B., de Jong, N. & Lohse D. 2010 Microbubble shape oscillations excited through ultrasonic parametric driving. *Phys. Rev.* E **82**, 026321.

Vogel, A., Lauterborn, W. & Timm, R. 1989 Optical and acoustic investigations of the dynamics of laser-produced cavitation bubbles near a solid boundary. *J. Fluid Mech.* **206**, 299–338.

Yasui, K. 1995 Effects of thermal conduction on bubble dynamics near the sonoluminescence threshold. *J. Acoust. Soc. Am.* **98** (5), 2772–2782.

Zabolotskaya, E. A. 1984 Interaction of gas bubbles in a sound wave field. *Sov. Phys. Acoust.* **30**, 365–368.

https://doi.org/10.1017/S0022112010006361 Published online by Cambridge University Press